CrossMark

RESEARCH PAPER

Fully coupled hydro-mechanical numerical manifold modeling of porous rock with dominant fractures

Mengsu Hu[1,2] · Yuan Wang[1,2] · Jonny Rutqvist[2]

Abstract Coupled hydro-mechanical (HM) processes are significant in geological engineering such as oil and gas extraction, geothermal energy, nuclear waste disposal and for the safety assessment of dam foundations and rock slopes, where the geological media usually consist of fractured rock masses. In this study, we developed a model for the analysis of coupled hydro-mechanical processes in porous rock containing dominant fractures, by using the numerical manifold method (NMM). In the current model, the fractures are regarded as different material domains from surrounding rock, i.e., finite-thickness fracture zones as porous media. Compared with the rock matrix, these fractured porous media are characterized with nonlinear behavior of hydraulic and mechanical properties, involving not only direct (poroelastic) coupling but also indirect (property change) coupling. By combining the potential energy associated with mechanical responses, fluid flow and solid–fluid interactions, a new formulation for direct HM coupling in porous media is established. For indirect coupling associated with fracture opening/closure, we developed a new approach implicitly considering the nonlinear properties by directly assembling the corresponding strain energy. Compared with traditional methods with approximation of the nonlinear constitutive equations, this new formulation achieves a more accurate representation of the nonlinear behavior. We implemented the new model for coupled HM analysis in NMM, which has fixed mathematical grid and accurate integration, and developed a new computer code. We tested the code for direct coupling on two classical poroelastic problems with coarse mesh and compared the results with the analytical solutions, achieving excellent agreement, respectively. Finally, we tested for indirect coupling on models with a single dominant fracture and obtained reasonable results. The current poroelastic NNM model with a continuous finite-thickness fracture zone will be further developed considering thin fractures in a discontinuous approach for a comprehensive model for HM analysis in fractured porous rock masses.

Keywords Direct coupling · Finite-thickness fracture zone · Fractured porous rock mass · Hydro-mechanical processes · Indirect coupling · Numerical manifold method

✉ Yuan Wang
wangyuanhhu@163.com;
wangyuan@hhu.edu.cn

Mengsu Hu
mengsuhu@lbl.gov

Jonny Rutqvist
jrutqvist@lbl.gov

1 College of Civil and Transportation Engineering, Hohai University, Nanjing 210098, China

2 Energy Geosciences Division, Lawrence Berkeley National Laboratory, Berkeley, CA 94720, USA

1 Introduction

Hydro-mechanical (HM) coupling refers to the interaction between hydraulic and mechanical processes that may be triggered by mechanical loading/unloading or fluid injection/extraction. This interaction is significant in geological engineering, such as oil and gas extraction, geothermal energy, nuclear waste disposal and for the safety assessment of dam foundation and rock slopes where the geological media usually consist of fractured rock [26]. These fractured rock masses may contain fractures with complex

geometry and fillings and thus could be modeled as a fractured porous media. Basically, the mechanisms of HM coupling in fractured porous media may be categorized as direct and indirect couplings [26]. Direct coupling is associated with the instantaneous undrained (pore volume) coupling between mechanical and hydraulic fields. Specifically, the fluid pressure changes instantaneously induce deformation, while the volume change instantaneously induces changes in fluid pressure. Indirect coupling refers to interaction between mechanical and hydraulic fields indirectly, through changes in material properties. Specifically, the effective stress changes, affected by fluid pressure changes, would change the stiffness of fractures, while the deformation of fractures changes their hydraulic conductivities [26, 35].

Since the early 1980s, a number of numerical models have been developed for modeling coupled hydro-mechanical processes in fractured rock. In 1982, Noorishad et al. [21] presented a finite element model for the coupled HM processes in deformable fractured rock masses. In that model, the constitutive relationships for the nonlinear deformable fractures were formulated, which was comparable to Biot's equations [3] for porous media. After that, increasing engineering demand has inspired development of many computer codes capable of modeling HM behavior of fractured rock at various levels of sophistication [29], including ROCMAS [22]; THAMES [23, 24], MOTIF [9], FRACON [19, 20], FEMH [4] applied in analysis of nuclear waste disposal; FRIP [25], FRACture [15] and GEOCRACK [33] applied in analysis of geothermal energy; and models applied for HM analysis of slopes and dam foundations (Wang et al. [34, 36, 37]). Most of the aforementioned models were developed based on the finite element method. With the development of discontinuous methods, fractures could be explicitly represented as a displacement discontinuity as they are modeled as interfaces of individual blocks. This includes both codes based on the models based on the distinct element method, including the commercially available UDEC [11] and 3DEC [12] codes, and models based on discontinuous deformation analysis (DDA), which may include coupled fluid flow and deformations in discrete fractures, but with the blocks between fractures assumed impermeable [13, 14]. Later, models based on the enriched finite element method were developed, such as a model in literature [32], in which simplified jump terms were constructed to realize the mechanical displacement discontinuity and hydraulic pressure continuity associated with fractures, whereas indirect coupling was not considered.

In order to realize the fully coupled HM processes in fractured porous media and to consider both direct and indirect couplings involving high nonlinearity and discontinuity, we explore and develop a model within the framework of the numerical manifold method (NMM). NMM is a numerical method based on the theory of mathematical manifolds invented by Shi [30, 31] and has been successfully applied to both continuous and discontinuous media in rock mechanics [5, 17]. The numerical meshes of NMM consist of two types of finite covers: mathematical covers and physical covers. Mathematical covers consist of finite overlapping covers that occupy the entire material domain and define the approximation precision. Conventional meshes such as regular finite difference grids, finite elements or convergence regions of series can be used as mathematical covers, whereas physical covers are divided by boundaries or joints from mathematical covers and define the integration domain. The global function of an element is the weighted average of the function on each physical cover overlapping an element. Thus, the NMM is flexible and general enough to include and combine well-developed analytical methods, the widely used FEM and block-oriented DDA, all in a unified form. Based on above definition, fluid flow models using NMM were developed, such as for analysis of free-surface flow [38] and flow in heterogeneous media [10]. For coupled HM problems in fractured rock, the following features of the NMM can be highlighted: (1) For large deformation, the NMM based on finite covers can model large deformation using fixed mathematical meshes [17, 30]; (2) for local small-scale fractures, the global approximation field can be easily enhanced by increasing the order of the physical cover functions from spatially constant (as in the finite element method) to linear or even defined by arbitrary user-defined functions [5]; (3) for complex fracture geometries or compositions, the simplex integration used in NMM [31] achieves exact analytical solutions in polygons with complex shapes. NMM modeling of coupled HM problems such as consolidation [16] or consolidation under dynamic loading [40] in porous media was developed, involving direct coupling.

In this study, we first provide a mathematical statement of the problem in Sect. 2. Based on the energy-work model for coupling mechanical and analysis, and considering finite-thickness fractures as continuous porous media, we develop a new formulation for considering both direct and indirect couplings in fractured porous rock, in Sect. 3. With the new formulation, we then establish a new model based on NMM in Sect. 4. In Sect. 5, we demonstrate our model for both direct and indirect couplings with several examples.

2 Mathematical statement of the problem

To describe the coupled HM behavior in porous deformable media, Biot established a general theory of 3D consolidation in 1941 [3], expressed as:

$$\nabla \cdot \boldsymbol{\sigma} + \mathbf{f} = \mathbf{0} \tag{1}$$

$$\nabla \cdot \mathbf{v} + \alpha \frac{\partial \varepsilon_v}{\partial t} + \frac{\gamma}{M} \frac{\partial h}{\partial t} = 0 \tag{2}$$

where $\boldsymbol{\sigma}$ is total stress tensor, $\mathbf{f}$ is body force vector, $\mathbf{v}$ is the fluid velocity vector, α is the Biot–Willis coefficient (usually ranges between 0 and 1), ε_v is the volumetric strain of the porous media, M is Biot's modulus, γ is the unit weight of the fluid, and h is the fluid hydraulic head, as the sum of fluid pressure head p and the head associated with elevation. Equation (1) represents the static mechanical equilibrium, and Eq. (2) represents the mass balance for fluid flow. These two equations are coupled through fluid pressure head p and volumetric strain ε_v. The Biot–Willis coefficient as a factor multiplied to fluid pressure in Eq. (1) signifies a modification and generalization of Terzaghi's effective stress law to:

$$\boldsymbol{\sigma} = \sigma' - \mathbf{m}\alpha\gamma p \tag{3}$$

where $\boldsymbol{\sigma}'$ is the effective stress tensor, $\mathbf{m}^\mathrm{T} = [1, 1, 1, 0, 0, 0]$ for 3D analysis or $\mathbf{m}^\mathrm{T} = [1, 1, 0]$ for 2D analysis. This theory for describing coupled HM responses in porous media was then widely used in its original form or in extension formulations for the modeling of porous deformable media, with linear or nonlinear properties.

For mechanical analysis of linear elastic porous media, we have:

$$\sigma' = \mathbf{E}\varepsilon \tag{4}$$

where $\mathbf{E}$ is the elastic constitutive tensor and $\boldsymbol{\varepsilon}$ is the strain tensor, which could be expressed in terms of displacements for small-deformation analysis as follows:

$$\boldsymbol{\varepsilon} = \mathbf{A}\mathbf{u} \tag{5}$$

where $\mathbf{A}$ is the strain–displacement matrix

$$\mathbf{A} = \begin{pmatrix} \dfrac{\partial}{x} & 0 \\ 0 & \dfrac{\partial}{y} \\ \dfrac{\partial}{y} & \dfrac{\partial}{x} \end{pmatrix} \tag{6}$$

and $\mathbf{u}$ is the displacement vector. For fluid flow in porous media, we assume that the fluid flow satisfies Darcy's law:

$$\mathbf{v} = -\mathbf{K}\mathrm{grad}(h) \tag{7}$$

where $\mathbf{K}$ is the tensor of permeability coefficient.

For rock fractures, linear elasticity according to Eq. (4) is not sufficient to describe the mechanical behavior, because it may be nonlinear elastic depending on effective stress. Goodman [7] described the normal closure (closing deformation normal to the fracture) as being inversely proportional to the effective normal stress. Then Bandis introduced

a constant to represent the zero-stress state of the fracture [2]. Here following Rutqvist et al. [27, 28], we use a reformulation of Bandis' [2] equation in terms of a mechanical aperture b_m which then is inversely proportional to the effective normal stress σ_n', according to (Fig. 1):

$$\sigma_n' = \frac{\xi}{b_\mathrm{m}} + \sigma_{n0}' \tag{8}$$

where σ_{n0}' is related to a Bandis' parameter, which is user-defined, and ξ is a constant defined as:

$$\xi = b_{\mathrm{m}i}\left(\sigma_{ni}' - \sigma_{n0}'\right) \tag{9}$$

where σ_{ni}' and $b_{\mathrm{m}i}$ are the effective normal stress and mechanical aperture at the initial or a reference state. Moreover, in Fig. 1, b_{mr} is a residual mechanical aperture that can remain open (incompletely closed) even at very high effective normal stress [27].

The relationship between shear displacement and shear stress for a rock fracture as have been observed in shear tests conducted under constant normal stress can according to Goodman's classical model [8] be characterized by elastic, peak and plastic regions as depicted in Fig. 2a. The peak shear stress σ_{sp} is equivalent to the peak shear strength, while the minimum post-peak shear stress σ_{sr} is the residual strength. In the elastic region, the shear stiffness is constant and independent of the normal stress, but both σ_{sp} and σ_{sr} increase with increasing normal stress, as shown in Fig. 2b. The linear shear stress–displacement relationship is expressed as:

$$\Delta\sigma_s' = k_s\Delta u_s \tag{10}$$

In order to be consistent with the relationship for normal closure behavior in Eq. (8), we introduce the following
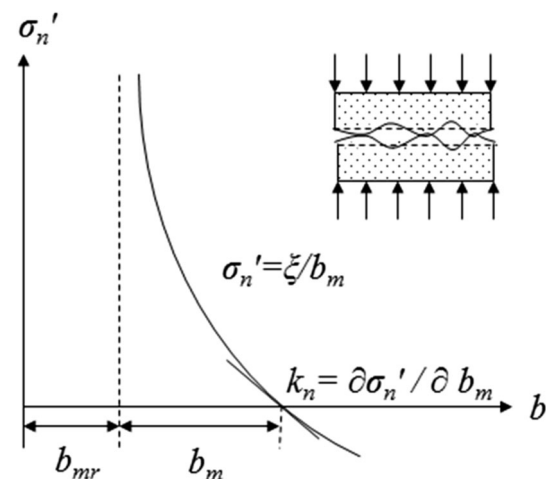

Fig. 1 Mechanical constitutive model: relationship between normal effective stress and aperture (Bandis et al. [2], Rutqvist et al. [28])
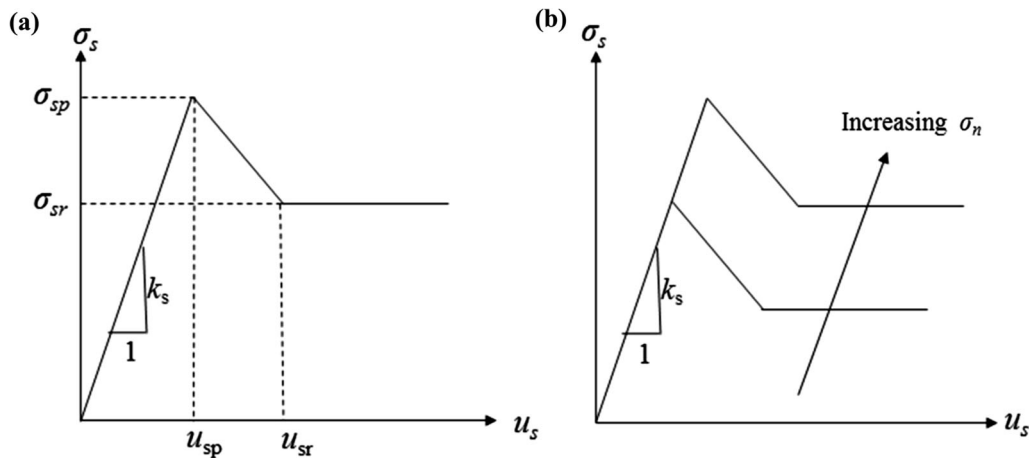
Fig. 2 Mechanical constitutive model: **a** relationship between shear stress and shear displacement. **b** Effect of normal stress σ on the relationship between shear stress and shear displacement (Goodman [8])

relationship to describe the behavior of fracture shear displacement under shear stress:

$$\sigma_s' = \frac{\Delta u_s}{\varsigma + \psi \Delta u_s} \tag{11}$$

where ς and Ψ are constants. Equation (11) was originally used to describe the nonlinear stress–strain behavior of soil [6]. Examining Eq. (11) we find that when $\Psi = 0$, the linear behavior is also included. We shall implement this equation for fracture shear behavior in our code for being consistent with the model for fracture normal mechanical behavior.

For fluid flow in fractures, the hydraulic conductivity k_f of a fracture depends on the size of interconnected voids between the two fracture surfaces and is related to a hydraulic fracture aperture b_h that can be defined according to Witherspoon et al. [39]:

$$k_f = \frac{b_h^2 \rho_f g}{12 \mu_f} \tag{12}$$

where ρ_f and μ_f are the fluid density and dynamic viscosity, and g is the gravitational acceleration, respectively. As the hydraulic and mechanical apertures could be very different [27], in Eq. (12), the hydraulic aperture b_h is assumed to be:

$$b_h = b_{hr} + f b_m \tag{13}$$

where b_{hr} is the residual hydraulic aperture when the fracture is mechanically closed and f is a factor that compensates for the deviation of flow in a natural rough fracture from the ideal parallel smooth fracture surfaces.

The boundary and initial conditions for the fractured porous rock masses are:

$$\mathbf{u} = \bar{\mathbf{u}} \quad \text{on } \Gamma_u \tag{14}$$

as given displacement boundary condition,

$$\boldsymbol{\sigma} \cdot \mathbf{n} = \bar{\mathbf{t}} \quad \text{on } \Gamma_t \tag{15}$$

as given traction boundary condition,

$$\mathbf{p} = \bar{\mathbf{p}} \quad \text{on } \Gamma_p \tag{16}$$

as given pressure head boundary condition,

$$\mathbf{v} \cdot \mathbf{n} = \bar{\mathbf{q}} \quad \text{on } \Gamma_v \tag{17}$$

as given specific discharge condition and

$$\mathbf{u}(\mathbf{x}, 0) = \mathbf{u_0}(\mathbf{x}) \quad \text{in } \Omega \tag{18}$$

$$\sigma(\mathbf{x}, 0) = \boldsymbol{\sigma_0}(\mathbf{x}) \quad \text{in } \Omega \tag{19}$$

$$\mathbf{p}(\mathbf{x}, 0) = \mathbf{p_0}(\mathbf{x}) \quad \text{in } \Omega \tag{20}$$

as initial conditions of displacement, stress and fluid pressure head, respectively.

3 Development of a new model for coupled HM analysis in fractured porous media

In this section, using an energy-work model for coupled HM analysis, we first derive the equilibrium equations for coupled behavior in porous media (Sect. 3.1). For fractured porous media (e.g., fractured rock masses), where indirect coupling is more significant, we then derive a new formulation for considering the fracture stiffness change in an accurate, implicit approach (Sect. 3.2).

3.1 An energy-work model for coupled HM analysis in porous media

In Ref. [30], Shi established the total potential energy associated with each component of dynamic/static mechanical processes, under point/surface/body loadings, possibly involving discontinuous and large deformation.

In Ref. [38] for fluid flow analysis, Wang et al. developed an energy-work seepage model for fluid flow analysis, considering all the work done by fluid flow in porous media. Later in order to better model Dirichlet boundary conditions and material interfaces for fluid flow problems, Hu et al. [10] developed a Lagrange multiplier method. Herein, the energy-work seepage model [38] is extended to conduct coupled HM analysis, linked by "work." By combining the work associated with mechanical responses, the work associated with fluid flow and the work associated with solid–fluid interactions, a new formulation for direct HM coupling in porous media is established.

3.1.1 The work associated with mechanical responses

The work associated with mechanical responses in terms of strain energy, initial stress, point loading, surface loading, body loading and given displacement boundary condition was derived by Shi [30]. They are as follows:

1. The strain energy Π_e for elastic rock is expressed as:

$$\Pi_e = \int_\Omega \int_0^\varepsilon \boldsymbol{\sigma}'^{\mathbf{T}} \mathrm{d}\varepsilon \mathrm{d}\Omega \tag{21}$$

2. The work W_σ associated with initial stress is expressed as:

$$W_\sigma = \int_\Omega \boldsymbol{\varepsilon}^{\mathbf{T}} \boldsymbol{\sigma}_0' \mathrm{d}\Omega \tag{22}$$

3. The work done by point loading W_p is:

$$W_\mathrm{p} = \mathbf{u}^{\mathbf{T}} \mathbf{F} \tag{23}$$

4. The work done by surface loading W_t is:

$$W_\mathrm{t} = \int_{\Gamma_\mathrm{t}} \mathbf{u}^{\mathbf{T}} \mathbf{F}_\mathrm{s} \mathrm{d}\Gamma_\mathrm{t} \tag{24}$$

5. The work done by body loading W_b is:

$$W_\mathrm{b} = \int_\Omega \mathbf{u}^{\mathbf{T}} \mathbf{F_b} \mathrm{d}\Omega \tag{25}$$

6. The work associated with given displacement boundary condition W_gd is expressed as

$$W_\mathrm{gd} = -\frac{1}{2} g_0 (\mathbf{u} - \bar{\mathbf{u}})^{\mathbf{T}} (\mathbf{u} - \bar{\mathbf{u}}) \tag{26}$$

using the penalty method [30] and assuming the stiffness g_0 of the penalty spring.

For discontinuous analysis of fractures as strong discontinuities, Shi [30] developed the algorithms for contact detection, open–closed iteration and contact enforcement and derived the work associated with contact between discontinuities. For dynamic analysis, the work associated with inertia is also considered. In this study, fractures are treated as porous media with nonlinear features under steady mechanical states. Therefore, the work associated with strong discontinuities and dynamic processes is deactivated.

3.1.2 The work associated with fluid flow

Based on an energy-work seepage model [38] for fluid flow analysis, the work associated with fluid flow in porous media, including domain flow, fluid gravity, was derived. Combined with a Lagrange multiplier method [10], the Dirichlet and Neumann boundary conditions can be imposed with unconstructed mesh and the associated work was also derived. Therefore, we can represent all the components of work associated with fluid flow in terms of the domain flow, fluid gravity and boundary conditions as follows.

1. The work associated with domain flow in porous media is expressed as:

$$W_\mathrm{s} = \gamma \int_\Omega \mathbf{v}^{\mathbf{T}} \nabla \mathbf{h} \mathrm{d}\Omega + 2\gamma \int_\Omega \frac{\partial h}{\partial t} \nabla \cdot \mathbf{v} \mathrm{d}\Omega \mathrm{d}t - \gamma \int_\Omega \boldsymbol{\theta} \mathrm{d}\mathbf{v} \mathrm{d}\Omega \tag{27}$$

where $\boldsymbol{\theta}$ is a choice vector $(0, 1)$ denoting the gravity direction. Substituting Eq. (2) into Eq. (27), we have:

$$W_\mathrm{s} = -\gamma \int_\Omega \nabla \mathbf{p}^{\mathbf{T}} \mathbf{K} \nabla \mathbf{p} \mathrm{d}\Omega - 2\gamma \int_\Omega \theta \mathbf{K} \nabla \mathbf{p} \mathrm{d}\Omega$$
$$- 2\gamma \int_\Omega \frac{\partial p}{\partial t} \left(\alpha \frac{\partial \varepsilon_v}{\partial t} + \frac{1}{M} \frac{\partial p}{\partial t} \right) \mathrm{d}\Omega \mathrm{d}t - \gamma \int_\Omega \boldsymbol{\theta} \mathrm{d}\mathbf{v} \mathrm{d}\Omega \tag{28}$$

Regardless of the effect of solid deformation, for work associated with fluid flow in porous media, we have:

$$W_\mathrm{s} = -\gamma \int_\Omega \nabla \mathbf{p}^{\mathbf{T}} \mathbf{K} \nabla \mathbf{p} \mathrm{d}\Omega - 2\gamma \int_\Omega \theta \mathbf{K} \nabla \mathbf{p} \mathrm{d}\Omega$$
$$- 2\gamma \int_\Omega \frac{\partial p}{\partial t} \frac{1}{M} \frac{\partial p}{\partial t} \mathrm{d}\Omega \mathrm{d}t - \gamma \int_\Omega \boldsymbol{\theta} \mathrm{d}\mathbf{v} \mathrm{d}\Omega \tag{29}$$

2. The work done by fluid gravity is:

$$W_\mathrm{g} = \gamma \int_\Omega \boldsymbol{\theta} \mathrm{d}\mathbf{v} \mathrm{d}\Omega \tag{30}$$

3. The work associated with Dirichlet boundary condition is expressed as:

$$W_\mathrm{D} = -\gamma \int_{\Gamma_\mathrm{D}} \mathbf{n}^{\mathbf{T}} \mathbf{K} \left(\nabla \mathbf{p}^{\mathbf{T}} + \boldsymbol{\theta}^{\mathbf{T}} \right) (\mathbf{p} - \bar{\mathbf{p}}) \mathrm{d}\Gamma_\mathrm{D} \tag{31}$$

using the Lagrange multiplier method developed in [10].

4. The work associated with Neumann boundary condition is:

$$W_\mathrm{N} = \gamma \int_{\Gamma_\mathrm{N}} \bar{\mathbf{q}}^{\mathbf{T}} (\mathbf{p} + \mathbf{y}) \mathrm{d}\Gamma_\mathrm{N} \tag{32}$$

3.1.3 The work associated with the fluid–solid interactions in porous media

Now we extend the energy-work seepage model [38] for coupled HM analysis by deriving the work associated with solid–fluid interactions. They are derived and explained as follows.

1. The work done by the fluid flow on solid deformation is obtained directly from the excess fluid pressure compared to the initial fluid pressure:

$$W_{\text{fs}} = \gamma \int_{\Omega} \alpha (\mathbf{p} - \mathbf{p_0})^{\mathbf{T}} \mathbf{m}^{\mathbf{T}} \varepsilon \, \mathrm{d}\Omega \tag{33}$$

2. The work done by solid deformation on fluid flow is obtained by considering how the solid deformation influences the mass balance of fluid flow. From Eq. (27) we can see that the work associated with solid deformation on fluid flow could be expressed as:

$$W_{\text{sf}} = -2\gamma \int_{\Omega} \frac{\partial p}{\partial t} \alpha \frac{\partial \varepsilon_{\text{v}}}{\partial t} \, \mathrm{d}\Omega \mathrm{d}t \tag{34}$$

Examining the expressions in this section, we see that all the components of "work" together are consistent with Biot's equations and corresponding boundary and initial conditions. The energy-work model provides a unique way to transform differential equations to integral equations with "work" as a bridge to link mechanical to fluid flow analysis.

3.2 A new approach to consider the indirect coupling in fractured porous media

In fractured rock masses, the main flow feature is seldom a simple plane single fracture, but may be a complex geological feature, consisting of multiple branching fractures intermingled with mineral-filled sections and damaged host rocks adjacent to fracture surfaces (Fig. 3a). The basic property of such a flow feature is its ability to conduct water along open and connected fracture parts, with a very sensitive relationship between fracture aperture and hydraulic conductivity as in Eq. (12). Another related key property is the nonlinear relationship between stress and fracture aperture as illustrated in Fig. 1. Moreover, such a flow feature is also associated with a mechanical weakness that may allow for in-elastic shear slip along its plane. One pragmatic approach to model such a flow feature is to simplify it as a finite-thickness equivalent porous deformable medium, which has strongly nonlinear properties reflecting inherent fracture flow and nonlinear fracture opening and/or shear behavior, with consideration of effects of fracture filling. The thickness of this equivalent porous media flow feature in the model may far exceed the real fracture width including open fracture parts and filling. It can include part of the host rock on each side of the flow feature, still retaining the key features of potential fracture flow and nonlinear deformation behavior. The model for such a flow feature is depicted in Fig. 3b. It is a porous medium of thickness I_d which includes both a dominant fracture flow path and other materials such as fracture filling
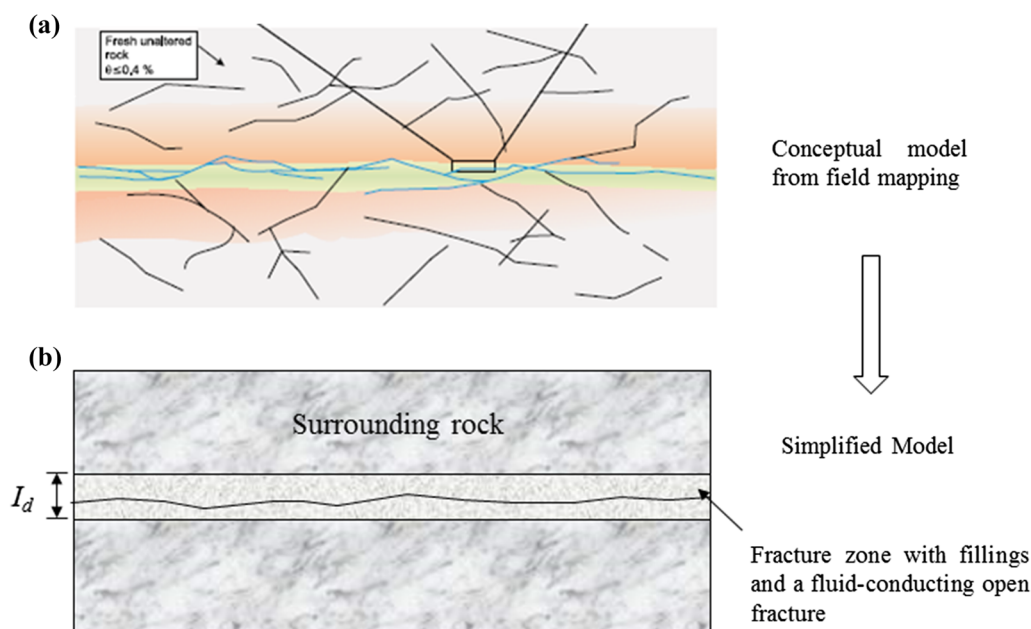

Fig. 3 Schematic of the simplified porous fractured rock model

and part of the host rock. For the dominant fracture flow path we consider its aperture for calculating the hydraulic conductivity, whereas the deformation behavior is affected by the nonlinear behavior of the fracture described in Eq. (8) as well as by the solid fracture fillings and adjacent host rock described to have linear elastic properties. As the fracture zones are modeled as porous media with different nonlinear properties from the surrounding rock, the boundaries of the fracture zones are regarded as material interfaces. The displacement continuity across these material interfaces are realized by penalty method [30], and the continuity of hydraulic head as well as the normal flux is realized by the Lagrange multiplier method developed by the authors in [10].

In the following we loosely define such a flow feature as a fracture zone. In this approach, we use an equivalent concept to represent this material behavior as follows:

$$\varepsilon_n^{(ii)} = \eta \delta \sigma_n'^{(ii)} + \frac{b_m^{(ii)} - b_m^{(ii-1)}}{I_d^{(ii-1)}} \tag{35}$$

Combining Eq. (8), Eq. (35) becomes:

$$\varepsilon_n^{(ii)} = \eta \delta \sigma_n'^{(ii)} + \frac{\dfrac{\xi}{\sigma_n'^{(ii)} - \sigma_{n0}'} - \dfrac{\xi}{\sigma_n'^{(ii-1)} - \sigma_{n0}'}}{I_d^{(ii-1)}} \tag{36}$$

where η represents the compliance of fillings and adjacent host rock within the fracture zone. Note that the nonlinear behavior of the fracture could be very strong (see Fig. 1) so that we use an incremental algorithm to express and solve for displacement and stress.

Based on the above concept, in this model, we develop a new formulation accounting for the nonlinear behavior of the finite-thickness fracture zone. Specifically, the nonlinear mechanical behavior of the fracture zone intrinsically influences the strain energy that could be stored in the material under deformation. Therefore, we directly introduce those nonlinear relationships to energy strain as described in the following subsections for normal and shear deformation.

3.2.1 An implicit approach to consider the normal stiffness change with effective stress

The normal constitutive model expressed in Eq. (36) could be rewritten as:

$$\sigma_n'^{(ii)} = \frac{\left[\eta\left(\sigma_n'^{(ii-1)} + \sigma_{n0}'\right) + x\right]}{2\eta} - \frac{\sqrt{\left[\eta\left(\sigma_n'^{(ii-1)} - \sigma_{n0}'\right) + x\right]^2 - 4\frac{\xi}{I_d^{(ii-1)}}\eta}}{2\eta} \tag{37}$$

where ii represents the iith time step; n denotes the local normal direction and

$$x = \varepsilon_n^{(ii)} + \frac{\xi}{\left[\sigma_{n0}'^{(ii-1)} - \sigma_{n0}'\right]I_d^{(ii-1)}} \tag{38}$$

Detailed derivation of the above equations can be found in "Appendix." The strain energy in the porous medium representing a fracture zone is expressed as:

$$\Pi_{\text{efn}} = \int_\Omega \int_0^{\varepsilon_n^{(ii)}} \sigma_n'^{(ii)} \mathrm{d}\varepsilon_n^{(ii)} \mathrm{d}\Omega \tag{39}$$

Combined with Eq. (37), Eq. (39) becomes:

$$\Pi_{\text{efn}} = \int_\Omega \int \frac{\left[\eta\left(\sigma_n'^{(ii-1)} + \sigma_{n0}'\right) + x\right]}{2\eta} \mathrm{d}x\mathrm{d}\Omega$$
$$- \int_\Omega \int \frac{\sqrt{\left[\eta\left(\sigma_n'^{(ii-1)} - \sigma_{n0}'\right) + x\right]^2 - 4\frac{\xi}{I_d^{(ii-1)}}\eta}}{2\eta} \mathrm{d}x\mathrm{d}\Omega \tag{40}$$

By integration with Taylor expansion, and projected into a local Cartesian fracture-zone coordinate system, Eq. (40) is expressed as:

$$\Pi_{\text{efn}} = \frac{1}{2\eta} \iint \left[\frac{1}{2} X_2^{(ii)} \left(\varepsilon_n^{(ii)}\right)^2 + X_1^{(ii)} \varepsilon_n^{(ii)}\right] \mathrm{d}s\mathrm{d}n \tag{41}$$

where the $X_1^{(ii)}$ and $X_2^{(ii)}$ are:

$$X_1^{(ii)} = \frac{\chi^{(ii-1)}}{I_d^{(ii-1)}} + \eta\left(\sigma_n'^{(ii-1)} + \sigma_{n0}'\right)$$
$$- \sqrt{\left[\eta\left(\sigma_n'^{(ii-1)} - \sigma_{n0}'\right) + \frac{\chi^{(ii-1)}}{I_d^{(ii-1)}}\right]^2 - 4\eta\frac{\xi}{I_d^{(ii-1)}}}$$

$$X_2^{(ii)} = 1 + \frac{-\left[\eta\left(\sigma_n'^{(ii-1)} - \sigma_{n0}'\right) + \frac{\chi^{(ii-1)}}{I_d^{(ii-1)}}\right]}{\sqrt{\left[\eta\left(\sigma_n'^{(ii-1)} - \sigma_{n0}'\right) + \frac{\chi^{(ii-1)}}{I_d^{(ii-1)}}\right]^2 - 4\eta\frac{\xi}{I_d^{(ii-1)}}}}$$

$$\chi^{(ii-1)} = \frac{\xi}{\sigma_n'^{(ii-1)} - \sigma_{n0}'} \tag{42}$$

According to coordinate transformation from global x–y to local s–n coordinate system, we have:

$$\varepsilon_n^{(ii)} = \mathbf{C}^{\mathbf{T}} \boldsymbol{\varepsilon}^{(ii)} \tag{43}$$

$$\mathrm{d}s\mathrm{d}n = \begin{vmatrix} \dfrac{\partial s}{\partial x} & \dfrac{\partial s}{\partial y} \\ \dfrac{\partial n}{\partial x} & \dfrac{\partial n}{\partial y} \end{vmatrix} \mathrm{d}x\mathrm{d}y = \mathbf{J}\mathrm{d}x\mathrm{d}y \tag{44}$$

where $\mathbf{C}^{\mathbf{T}} = (\sin^2\theta, \cos^2\theta, -\sin\theta\cos\theta)$. Then we finally obtain:

$$\Pi_{\text{efn}} = \frac{1}{2\eta} \iint \left[X_1^{(ii)} \mathbf{C^T}\boldsymbol{\varepsilon} + \frac{1}{2} X_2^{(ii)} \boldsymbol{\varepsilon}^{\mathbf{T}} \mathbf{C}\mathbf{C^T}\boldsymbol{\varepsilon} \right] \mathbf{J} dx dy \qquad (45)$$

3.2.2 An implicit approach to consider the fracture mechanical behavior in the shear direction

The shear constitutive model expressed by Eq. (11) could be further expressed as:

$$\sigma_s' = \frac{e_s^{(ii)}}{\varsigma / b_m^{(ii-1)} + \psi e_s^{(ii)}} \qquad (46)$$

where $e_s = \Delta u_s^{(ii)} / b_m^{(ii-1)}$.

Similar to the approach for fracture normal mechanical behavior, we directly express the associated strain energy as:

$$\Pi_{\text{efs}} = \int_{\Omega} \int_0^{e_s^{(ii)}} \sigma_s'^{(ii)} de_s^{(ii)} d\Omega \qquad (47)$$

Combined with Eq. (46), Eq. (47) becomes:

$$\Pi_{\text{efs}} = \int_{\Omega} \int_0^{e_s^{(ii)}} \frac{e_s^{(ii)}}{\varsigma / b_m^{(ii-1)} + \psi e_s^{(ii)}} de_s^{(ii)} d\Omega \qquad (48)$$

By integration, Eq. (48) becomes:

$$\Pi_{\text{efs}} = \int_{\Omega} \left[\frac{1}{\psi} e_s^{(ii)} - \frac{\varsigma / b_m^{(ii-1)}}{\psi^2} \ln\left(\varsigma / b_m^{(ii-1)} + \psi e_s^{(ii)} \right) \right] d\Omega \qquad (49)$$

By Taylor expansion, we have:

$$\ln\left(\varsigma / b_m^{(ii-1)} + \psi e_s^{(ii)} \right) = \psi b_m^{(ii-1)} / \varsigma e_s^{(ii)}$$
$$- \frac{1}{2}\left[\psi b_m^{(ii-1)} / \varsigma \right]^2 (e_s^{(ii)})^2$$
$$+ o(e_s^{(ii)}) + \ln\left(\varsigma / b_m^{(ii-1)} \right) \qquad (50)$$

Substituting Eqs. (50)–(49), and projecting into the local Cartesian fracture-zone coordinate system, we have:

$$\Pi_{\text{efs}} = \frac{1}{2} b_m^{(ii-1)} / \varsigma \iint \left(e_s^{(ii)} \right)^2 ds dn \qquad (51)$$

According to coordinate from global x–y to local s–n coordinate system, we have:

$$e_s^{(ii)} = \mathbf{C'^T}\mathbf{B'}u^{(ii)} \qquad (52)$$

$$ds dn = \begin{vmatrix} \dfrac{\partial s}{\partial x} & \dfrac{\partial s}{\partial y} \\ \dfrac{\partial n}{\partial x} & \dfrac{\partial n}{\partial y} \end{vmatrix} dx dy = \mathbf{J} dx dy \qquad (53)$$

where $\mathbf{C'^T} = (-\sin\theta\cos\theta,\ \sin\theta\cos\theta,\ \cos^2\theta,\ -\sin^2\theta)$ and

$$\mathbf{B'} = \begin{pmatrix} \dfrac{\partial}{x} & 0 & \dfrac{\partial}{y} & 0 \\ 0 & \dfrac{\partial}{y} & 0 & \dfrac{\partial}{x} \end{pmatrix}^{\mathbf{T}}.$$ Then we finally obtain:

$$\Pi_{\text{efs}} = \frac{1}{2} b_m^{(ii-1)} / \varsigma \iint u\mathbf{B'^T}\mathbf{C'^T}\mathbf{C'}\mathbf{B'}u\mathbf{J} dx dy \qquad (54)$$

3.2.3 Fluid flow in deformable porous fracture zones

The tensor of permeability coefficient $\mathbf{H}$ of the deformable porous fracture zones in local 2D coordinate system is expressed as:

$$\mathbf{H} = \begin{pmatrix} k_f & 0 \\ 0 & k_{fn} \end{pmatrix} \qquad (55)$$

where k_{fn} denotes the hydraulic conductivity in the normal direction. The work done by domain flow in the fractures is expressed as:

$$W_{\text{fs}} = -\gamma \int_{\Omega} \nabla\mathbf{p^T}\mathbf{H}\nabla\mathbf{p} d\Omega - 2\gamma \int_{\Omega} \theta\mathbf{H}\nabla\mathbf{p} d\Omega$$
$$- 2\gamma \int_{\Omega} \frac{\partial p}{\partial t} \frac{1}{M} \frac{\partial p}{\partial t} d\Omega dt - \gamma \int_{\Omega} \boldsymbol{\theta} d\mathbf{v} d\Omega \qquad (56)$$

After transforming from the local fracture-zone coordinate system to global Cartesian coordinate system, we have:

$$W_{\text{fs}} = -\gamma \int \nabla\mathbf{p^T}\mathbf{F^T}\mathbf{H}\mathbf{F}\nabla\mathbf{p}\mathbf{J} dx dy - 2\gamma \int \theta\mathbf{H}\mathbf{F}\nabla\mathbf{p}\mathbf{J} dx dy$$
$$- 2\gamma \int \frac{\partial p}{\partial t} \frac{1}{M} \frac{\partial p}{\partial t} \mathbf{J} dx dy dt - \gamma \int_{\Omega} \boldsymbol{\theta} d\mathbf{v} d\Omega \qquad (57)$$

where $\mathbf{F} = \begin{pmatrix} \cos\theta & \sin\theta \\ -\sin\theta & \cos\theta \end{pmatrix}$.

The other terms of work could be expressed in the same way as for porous media, under coordinate transformation from fractures-zone local coordinates to the global Cartesian coordinate system.

4 Coupled HM NMM analysis of fractured porous rock masses

4.1 Fundamentals of NMM

Here we briefly describe the fundamentals of NMM for both mechanical and fluid flow analysis, including mathematical covers, physical covers, elements, cover functions and weight functions. In this study, we use triangles to form mathematical covers, because of their proven good numerical performance
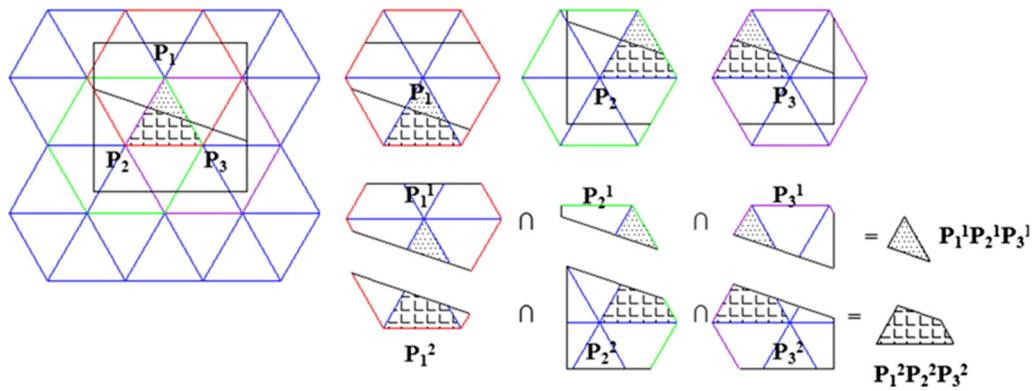
Fig. 4 Mathematical covers, physical covers and elements defined in NMM with uniform triangles as mathematical mesh

[1]. As shown in Fig. 4, all the triangles sharing a certain node (or 'star') form a mathematical cover (i.e., a hexagon such as P_1, P_2 and P_3, distinguished by different colors). The corresponding physical covers (P_1^1 and P_1^2, P_2^1 and P_2^2 and P_3^1 and P_3^2) are divided from the mathematical covers by boundaries, including material interfaces if they are regarded as discontinuities. The overlapping areas of physical covers are defined as elements (such as elements $P_1^1 P_2^1 P_3^1$ and $P_1^2 P_2^2 P_3^2$, distinguished in Fig. 4 by different fill patterns).

In NMM, the approximations of field variables (including displacements for mechanical analysis and pressure head for fluid flow analysis) within an element are the weighted average of functions on all physical covers overlapping this element. They are expressed as:

$$u = \mathbf{w_u^T u_{pc}} \tag{58}$$

$$p = \mathbf{w_p^T p_{pc}} \tag{59}$$

where u and p are the variables on a certain element, $\mathbf{u_{pc}}$ and $\mathbf{p_{pc}}$ are the vectors of physical cover functions of displacement and pressure head, and $\mathbf{w_u}$ and $\mathbf{w_p}$ are the vectors of weight functions of physical cover functions $\mathbf{u_{pc}}$ and $\mathbf{p_{pc}}$ on this element. For an individual physical cover i, we have

$$\begin{cases} w_u^i(x,y) > 0, \; w_p^i(x,y) > 0 & (x,y) \in U_i \\ w_u^i(x,y) = 0, \; w_p^i(x,y) = 0 & (x,y) \notin U_i \end{cases} \tag{60}$$

where U_i is the geometric range of physical cover i.

The cover functions $\mathbf{u_{pc}}$ and $\mathbf{p_{pc}}$ can be a series of any order:

$$\mathbf{u_{pc}} = \mathbf{f^T D} \tag{61}$$

$$\mathbf{p_{pc}} = \mathbf{s^T P} \tag{62}$$

where $\mathbf{f}$ and $\mathbf{s}$ are the vectors of the coefficients of the degrees of freedom (DOFs) $\mathbf{D}$ and $\mathbf{P}$ to be solved in mechanical and fluid flow fields, respectively. Specifically, $\mathbf{D}$ represents DOFs in terms of displacements and $\mathbf{P}$ represents DOFs in terms of pressure head. For 2D analysis, $\mathbf{f}$ and $\mathbf{s}$ are the subsets of vector $(1, x, y, x^2, y^2, xy, \ldots)^T$. For example in

standard finite element analysis with constant cover functions (called nodal values in FEM), $\mathbf{f}$ and $\mathbf{s}$ are the vectors $(1)^T$ and the number of DOFs m associated with a physical cover is 3 (2 for displacements and 1 for pressure head). For linear approximation of displacement, $\mathbf{f}$ could be written as $(1, x, y)^T$ and the associated DOFs of a physical cover in the mechanical field become 6. Substituting Eqs. (61) and (62) back to Eqs. (58) and (59), the contribution of each physical cover to all corresponding elements is summed to form the global approximation over the entire domain.

In this paper, we use linear weight functions and constant physical cover functions for both mechanical and fluid flow analysis with a triangular mesh. Note that even though Zienkiewicz et al. [41] indicated that T3/C3 elements failed in a patch test, we should note that Eq. (2) in [41] and the boundary conditions in the test are very different from the coupled HM problem in this work. Besides, the work presented in [42] showed that the correct assembling of the equilibrium equations for this problem could successfully overcome the restrictions of a mixed formulation.

4.2 NMM global equilibrium equations for coupled HM analysis

According to the energy-work theorem,

$$W_\varphi + \Pi_\varphi = 0 \tag{63}$$

we can derive the potential energy associated with each component associated with coupled HM processes in fractured rock masses. We further combine with NMM approximations expressed by Eqs. (49)–(53) and project the integration into a 2D Cartesian coordinate system and derive the potential energy for the solid as follows:

1. the strain energy for elastic porous rock is:

$$\Pi_e = \int_\Omega \mathbf{D^T B^T E B D} \, dxdy \tag{64}$$

where $\mathbf{B} = \mathbf{A w_u^T f^T}$.

2. the potential energy associated with initial stress is:

$$\Pi_\sigma = -\int_\Omega \mathbf{D^T B^T} \sigma'_0 \mathrm{d}x\mathrm{d}y \tag{65}$$

3. the potential energy associated with point loading is:

$$\Pi_\mathrm{p} = -\mathbf{D^T T^T F} \tag{66}$$

where $\mathbf{T} = \mathbf{w_u^T f^T}$.

4. the potential energy associated with surface loading is:

$$\Pi_t = -\int_{\Gamma_\mathrm{s}} \mathbf{D^T T^T F_s} d\Gamma_t \tag{67}$$

5. the potential energy associated with body loading is:

$$\Pi_\mathrm{b} = -\int \mathbf{D^T T^T F_b} \mathrm{d}x\mathrm{d}y \tag{68}$$

6. the potential energy associated with a given displacement boundary condition is:

$$\Pi_\mathrm{gd} = \frac{1}{2} g_0 \left(\mathbf{D^T T^T} - \mathbf{\bar{u}^T}\right)\left(\mathbf{TD} - \mathbf{\bar{u}}\right) \tag{69}$$

7. the potential energy associated with the work done by fluid flow on the solid is:

$$\Pi_\mathrm{fs} = -\gamma\alpha \int_\Omega \left(\mathbf{P^T O^T m^T BD} - \mathbf{p_0 m^T BD}\right)\mathrm{d}\Omega \tag{70}$$

here $\mathbf{O} = \mathbf{w_p^T s^T}$.

Also, we can derive the following potential energy for fluid flow:

1. The potential energy associated with domain flow in porous media is:

$$\Pi_\mathrm{s} = \gamma \int \left[\mathbf{P^T G^T KGP} + 2\theta\mathbf{KGP} \right. $$
$$\left. + \frac{2}{M\Delta}\left(\mathbf{P^T O^T OP} - \mathbf{P^T O^T \tilde{P}}\right)\right]\mathrm{d}x\mathrm{d}y + \gamma \int_\Omega \boldsymbol{\theta}\mathrm{d}\mathbf{v}\mathrm{d}\Omega \tag{71}$$

where $\mathbf{G} = (\partial/\partial x, \partial/\partial y)^\mathrm{T}\mathbf{O}$, $\tilde{\mathbf{P}}$ is the time-iteration choice for $\mathbf{P}$, and Δ is the time step, respectively.

2. The potential energy associated with fluid gravity is:

$$\Pi_\mathrm{g} = -\gamma \int_\Omega \boldsymbol{\theta}\mathrm{d}\mathbf{v}\mathrm{d}\Omega \tag{72}$$

3. The potential energy associated with Dirichlet boundary condition is:

$$\Pi_\mathrm{D} = \gamma \int_{\Gamma_\mathrm{D}} \mathbf{n^T K}\left(\mathbf{P^T G^T OP} + \boldsymbol{\theta^T OP} - \mathbf{P^T G^T \bar{p}} - \boldsymbol{\theta^T \bar{p}}\right)\mathrm{d}\Gamma_\mathrm{D} \tag{73}$$

4. The potential energy associated with Neumann boundary condition is:

$$\Pi_\mathrm{N} = -\gamma \int_{\Gamma_\mathrm{N}} \left(\mathbf{\bar{q}^T OP} + \mathbf{\bar{q}^T y}\right)\mathrm{d}\Gamma_\mathrm{N} \tag{74}$$

5. The potential energy associated with deformation effects on fluid flow is:

$$\Pi_\mathrm{sf} = \frac{2\alpha\gamma}{\Delta} \int \left(\mathbf{D^T B^T m^T OP} - \mathbf{\tilde{D}^T B^T m^T OP}\right)\mathrm{d}x\mathrm{d}y \tag{75}$$

where $\tilde{\mathbf{D}}$ is the time-iteration choice for $\mathbf{D}$.

For fracture zones modeled as deformable porous media where indirect coupling is manifested by changes in material properties with effective stress or deformation, we derive the following expressions:

1. The strain energy:

$$\Pi_\mathrm{ef} = \iint \left\{ \frac{1}{2\eta}\left[\mathrm{X}_1^{(ii)}\mathbf{C^T BD} + \frac{1}{2}\mathrm{X}_2^{(ii)}\mathbf{D^T B^T CC^T BD}\right] \right.$$
$$\left. + \frac{1}{2}b_\mathrm{m}^{(ii-1)}\Big/ \varsigma\mathbf{D^T T^T}\beta\mathbf{TD}\right\}\mathbf{J}\mathrm{d}x\mathrm{d}y \tag{76}$$

where $\boldsymbol{\beta} = \mathbf{B'^T C'^T C'B'}$

2. The potential energy associated with work done by domain flow

$$\Pi_{fs} = \gamma \int \left[\mathbf{P^T G^T F^T HFGP} + 2\theta\mathbf{HFGP}\right.$$
$$\left. + \frac{2}{M\Delta}\left(\mathbf{P^T O^T OP} - \mathbf{P^T O^T \tilde{P}}\right)\right]\mathbf{J}\mathrm{d}x\mathrm{d}y - \gamma \int_\Omega \boldsymbol{\theta}\mathrm{d}\mathbf{v}\mathrm{d}\Omega \tag{77}$$

The other expressions are similar to the expressions as for porous media after coordinate transformation from fracture-zone local to global coordinates.

Adding the potential energy component expressed by Eqs. (64)–(70) and Eqs. (71)–(75), we have the total potential energy Π^m for mechanical analysis and total potential energy Π^f for fluid flow analysis. The equilibrium equations are derived by minimization of the total potential energy for mechanics and fluid flow. Specifically, equation $\partial\Pi^\mathrm{m}/\partial d_i = 0$ represents the mechanical equilibrium on the ith physical cover and $\partial\Pi^\mathrm{f}/\partial p_i = 0$ represents the equilibrium of flux on the ith physical cover. The final equilibrium equation is expressed as:

$$\begin{pmatrix} \mathbf{N} & -\mathbf{S} \\ \dfrac{\mathbf{S^T}}{\Delta} & \mathbf{C} \end{pmatrix}\begin{pmatrix} \mathbf{D} \\ \mathbf{P} \end{pmatrix} = \begin{pmatrix} \mathbf{L} \\ \mathbf{Q} \end{pmatrix} \tag{78}$$

where N_{ij} is the element of matrix N, representing the mechanical contribution of physical cover j on physical cover i, derived by:

$$N_{ij} = \frac{\partial^2 \Pi^\mathrm{m}}{\partial d_i \partial d_j} \tag{79}$$

S_{ij} is the element of matrix $\mathbf{S}$, representing the contribution of fluid flow of physical cover j on deformation of physical cover i, derived by:

$$S_{ij} = \frac{\partial^2 \Pi^m}{\partial d_i \partial p_j} \qquad (80)$$

C_{ij} is the element of matrix $\mathbf{C}$, representing the fluid flow contribution of physical cover j on deformation of physical cover i, derived by:

$$C_{ij} = \frac{\partial^2 \Pi^f}{\partial p_i \partial p_j} \qquad (81)$$

L_j is the element of matrix $\mathbf{L}$, representing loading term and derived by:

$$L_j = -\frac{\partial \Pi^m}{\partial d_j} \qquad (82)$$

and flux term Q_j as the element of matrix $\mathbf{Q}$, derived by:

$$Q_j = -\frac{\partial \Pi^f}{\partial p_j} \qquad (83)$$

In the matrices N, L and C, Q, time step and previous time-step displacements and pressure heads may be included representing inertial and compression of the fluid–solid system, respectively. In the equilibrium Eq. (78), all the terms are calculated by simplex integration. Simplex integration, proposed by Shi [31], achieves analytical solution for polynomials over elements of arbitrary shape.

4.3 Time iteration

Following the original NMM for mechanical analysis by Shi [30], we use the implicit scheme. The reason is that the nonlinear behavior may be very strong, especially for the porous fractures, and thereby the changes between different time steps may be very large. So it is desirable to use implicit scheme for high accuracy. In each time step, the displacement increments and fluid pressure are calculated. After each time step, the displacements and initial stress are updated as follows:

$$\mathbf{D}^{(ii+1)} = \mathbf{D}^{(ii)} + \delta \mathbf{D}^{(ii+1)} \qquad (84)$$

The stress is calculated by Eq. (37).

For this nonlinear problem, we use a direct solver to solve the global equilibrium equations for faster convergence rate.

5 Demonstration examples

On the basis of the above formulation for coupled HM behavior in fractured rock masses, we developed a new computer code. To demonstrate the accuracy and computational efficiency of the NMM model and computer code, we employed four example problems: (1) a porous elastic column, (2) a porous elastic infinite-long layer, (3) a rock domain containing a dominant fracture and (4) a rock domain containing a fracture zone subject to constant pressure fluid injection. In the first two examples, we compare our modeling results with analytical solutions and present the results in terms of accuracy and convergence efficiency.

5.1 Example 1: modeling of direct HM coupling in a poroelastic column supporting vertical loading on the top

In order to demonstrate the efficiency and accuracy of the new NMM code for modeling coupled HM behavior of porous deformable media, we simulate the common verification example of a poroelastic column supporting vertical loading on the top boundary. We choose the same model geometry, boundary conditions and properties as in [16]. The model geometry and boundary conditions are shown in Fig. 5. The column is 80 m high and 20 m wide. The Young's modulus is 3.7×10^6 Pa, and the Poisson's ratio is 0.35. The permeability coefficient is 2×10^{-8} m/s. The loading is evenly applied on the top boundary of the column with a boundary stress of 200 kPa. First, we set an infinite Biot's modulus and use the developed NMM code with fixed mesh of different sizes when kv = 2, kv = 4, kv = 8 and kv = 16 to simulate this problem, where kv represents the half number of mesh layers. The mesh geometry of different mesh sizes is as shown in Fig. 6, and
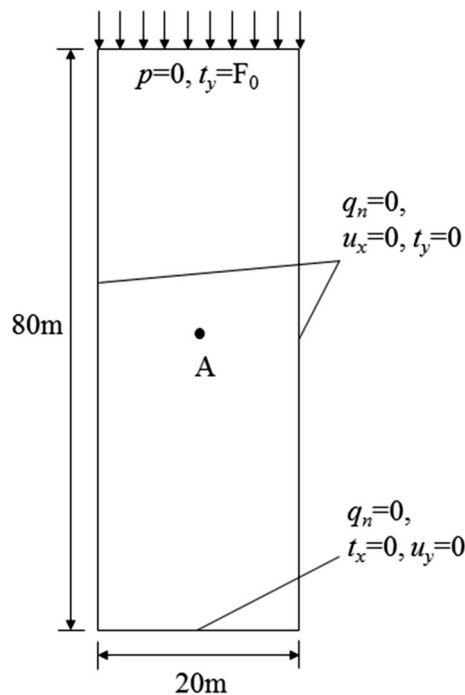

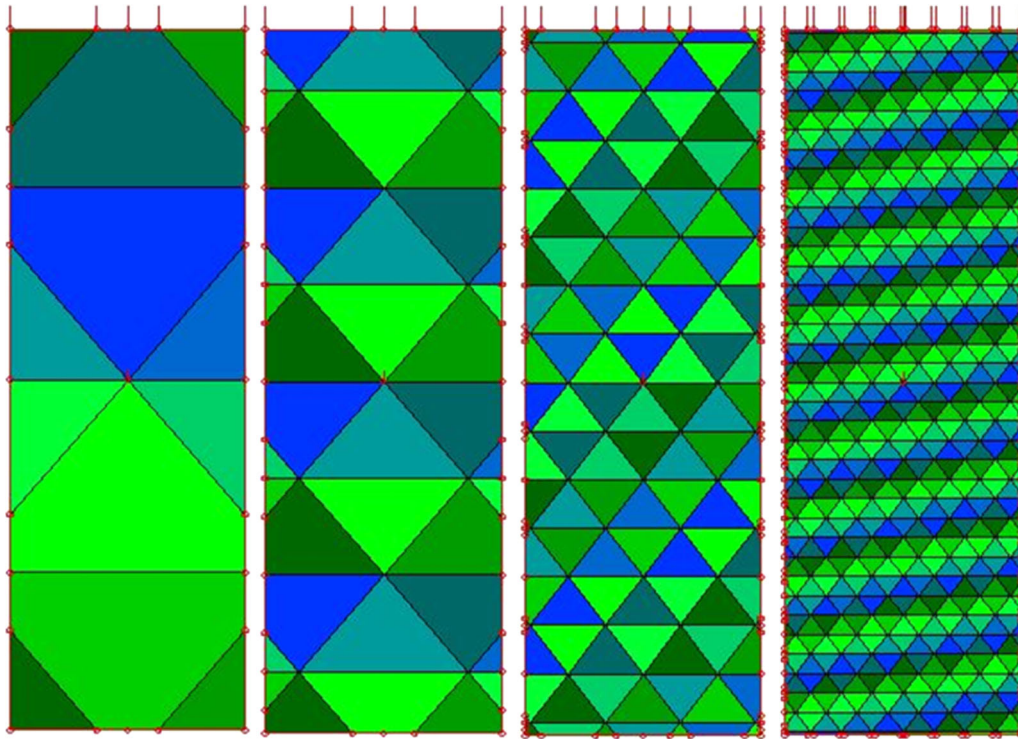Fig. 5 Model geometry and boundary conditions

Fig. 6 Mesh geometry with different sizes

Table 1 Comparison of computation parameters of different mesh sizes

	Number of element	Number of physical covers	Settlement (m)
kv = 2	12	13	−2.69362
kv = 4	40	31	−2.69352
kv = 8	144	93	−2.69348
kv = 16	642	367	−2.69339
Analytical solution [3]	–	–	−2.693841

kv is the half number of mesh layers

the computation parameters are listed in Table 1. As we can see the deviation of the calculated settlement from the analytical solution is no more than 0.02 %, herein the larger deviation with denser mesh may be due to small elements along the vertical boundaries, on which the given displacement boundary condition is realized by penalty method with large penalty spring stiffness.

The analytical solution of the settlement and the fluid pressure evolution for this problem was derived by Biot [3], expressed as:

$$w_{s}(t) = \frac{8}{\pi^2} a h_c F_0 \sum_{n=0}^{\infty} \frac{1}{(2n+1)^2} \left\{ 1 - e^{\left[-\left(\frac{(2n+1)\pi}{2h_c} \right)^2 ct \right]} \right\}$$

(85)

$$p(y,t) = \frac{4}{\alpha\pi} F_0 \sum_{n=0}^{\infty} \frac{1}{(2n+1)} e^{\left[-\left(\frac{(2n+1)\pi}{2h_c} \right)^2 ct \right]} \sin \frac{(2n+1)\pi y}{2h_c}$$

(86)

where h_c is the height of the column and a and c are the final compressibility and consolidation constants defined by Biot [3].

We compare the calculated results of the settlement evolution for different mesh sizes to the analytical solution in Eqs. (85) and (86). The time step we used for the simulation is 100 days, and the simulated time span is as long as 20,000 days. From Fig. 7a we see that even with the coarsest mesh using 4 layers and 12 elements, we could achieve excellent results. We further choose a point A located at (10, 40 m) and calculate the fluid pressure evolution and compare with the analytical solution according to Eq. (86). We find good agreement in Fig. 7b between the numerical results and the analytical solution, with slight deviation for the coarsest mesh involving only 12 elements (kv = 2). Furthermore, we study the sensitivity of the calculation with different choices of Biot's modulus. Figure 8 shows the evolution of settlement and fluid pressure with different values of Biot's modulus. Good agreement between analytical and numerical solutions, for example when the Biot's modulus is 6 MPa, verifies the accuracy for the transient problems involving Biot's modulus. As we can see, Biot's modulus may play an important role in this transient processes, slowing down
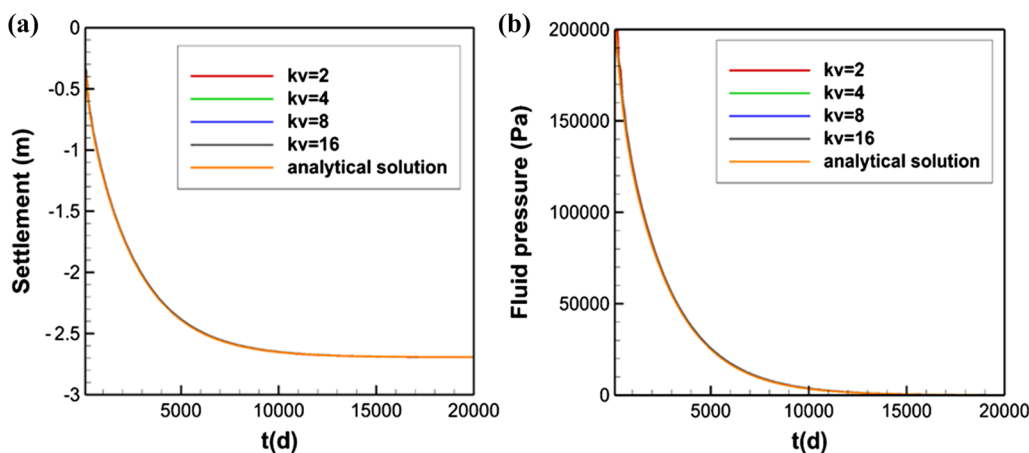
Fig. 7 Comparison of the calculated **a** settlement (m) and **b** fluid pressure (Pa) evolution with NMM using different sizes of mesh and the analytical solution by Biot [3]
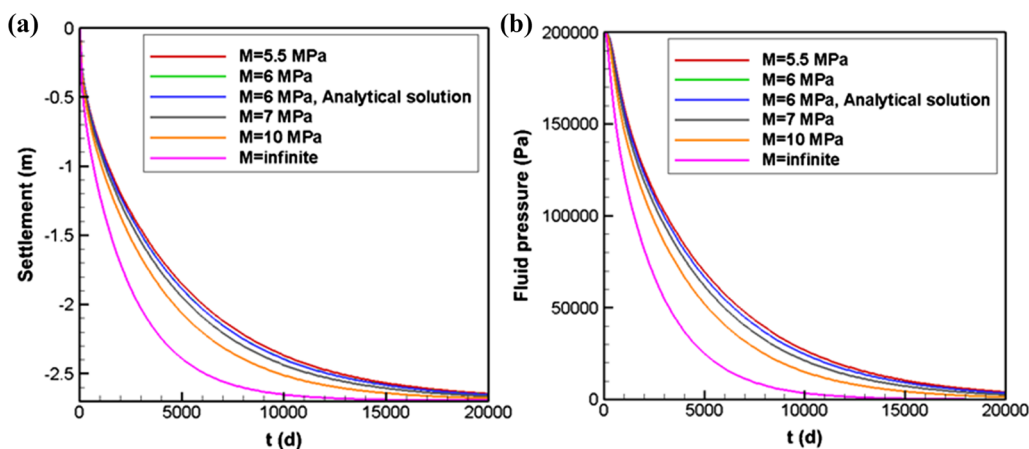

Fig. 8 Sensitivity of **a** settlement (m) and **b** fluid pressure (Pa) with the different choices of the Biot's modulus

the settlement and pressure dissipation process. With an increase of Biot's modulus, its influence on the coupled HM process is reduced. Specifically, if Biot's modulus is 20 MPa, its effect on this problem can be ignored. However, in order to eliminate the transient effect by Biot's modulus and focus on the fluid–solid interaction as a transient term, we set infinite values in other examples.

From this example, we show that our new NMM model for coupled HM modeling in porous media is accurate even when using a rather coarse mesh.

5.2 Example 2: modeling of direct coupled processes in an infinite poroelastic layer subjected to loading on the top face

Figure 9 shows a semi-infinite poroelastic media subjected to a 6-m-long strip loading with a stress magnitude of 20 kPa on the top face.

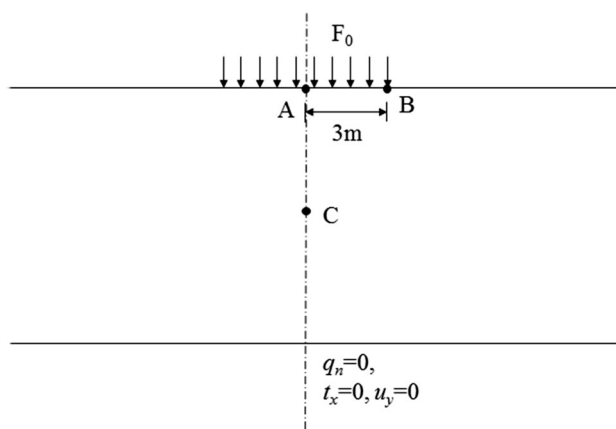We first choose the 100 m × 100 m numerical model with drained top boundary and impermeable bottom

Fig. 9 Model geometry and boundary conditions

boundary (Fig. 10a). The Young's modulus is 4 MPa, and the Poisson's ratio is 0. The permeability coefficient is 2.5×10^{-8} m/s. By symmetry we extract the right half of the model from the line passing through AC to simulate the
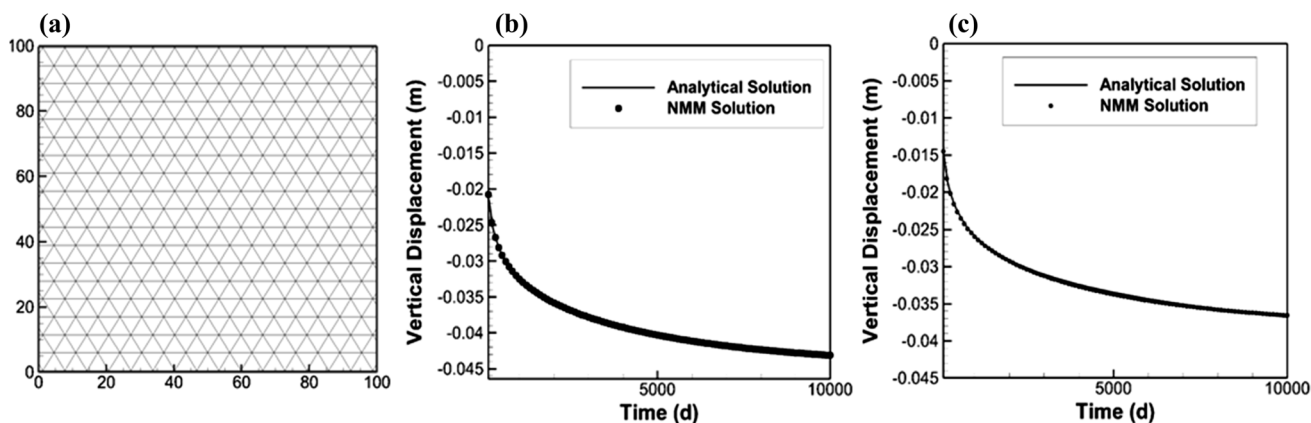
Fig. 10 a NMM mesh and comparison of the evolution of calculated vertical displacements at b point A and c point B with the analytical solution by McNamee and Gibson [18]
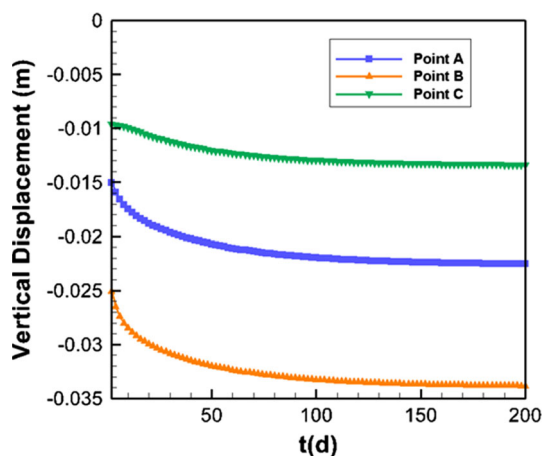

Fig. 11 Evolution of vertical displacement of points A, B and C

coupled HM behavior. Points A and B located at (0, 100) and (3, 100) are points used for comparison of numerical and analytical results. McNamee and Gibson [18] provided the analytical solution for this problem when the Poisson ratio is 0. We calculate the evolution of vertical displacements at points A and B using a coarse mesh (Fig. 10a) and compare with the analytical solution as shown in Fig. 10b, c. We see that our model result agrees very well with the analytical solution for this case.

Then we change the model dimension to 30 m wide and 12 m high with Poisson's ratio 0.3. We first calculate the evolution of vertical displacement at the three points A (0, 6), B (0, 12), C (3, 12), as shown in Fig. 11. Note that the points A, B and C are different from the ones shown in Fig. 9; therefore, the vertical displacement at point B is the largest. Furthermore, we output the fluid pressure distribution at different stages calculated by our NMM code, as shown in Fig. 12. From Fig. 12 we can clearly see the process of fluid pressure dissipation at different times.

5.3 Example 3: NMM modeling of direct and indirect coupled HM processes under vertical loading and fluid injection

In order to demonstrate the formulation for considering both direct and indirect coupled hydro-mechanical processes in rock with fractures, we simulate a rectangular rock domain containing a fracture zone subjected to instantaneous vertical loading and a constant pressure fluid injection. The model geometry, boundary conditions and the mesh are as shown in Fig. 13a, b, respectively. The material parameters are listed in Table 2. In this case, the initial thickness of the fracture zone is 0.1 m, whereas the mechanical fracture aperture for the assumed dominant fracture flow path is 1×10^{-4} m (0.1 mm) and with an equivalent hydraulic aperture of 5×10^{-5} m (50 μm). This is at an initial effective vertical stress of -8 MPa (a negative stress values signifies compressive stress) involving an initial total vertical stress of -8 MPa and a zero initial fluid pressure. Note that the given displacement boundary conditions and material interfaces for mechanical analysis are realized by the penalty method and the stiffness of the penalty spring g_0 is determined as suggested by Shi [30].

Since the developed nonlinear finite-thickness fracture-zone model is new and there is no available closed-form solution or numerical results for comparison of the transient HM response for this case, we run this simulation step-by-step to confirm that the results are reasonable. As the model development for fluid flow analysis was presented and verified previously [10] and the direct coupling was verified in Examples 1 and 2, here we focus on verification of the indirect coupling algorithms. First we applied the instantaneous vertical loading with magnitude of 10 MPa on the top of the model and conducted a mechanical analysis without fluid injection. This results in an instantaneous closure of the fracture considering its
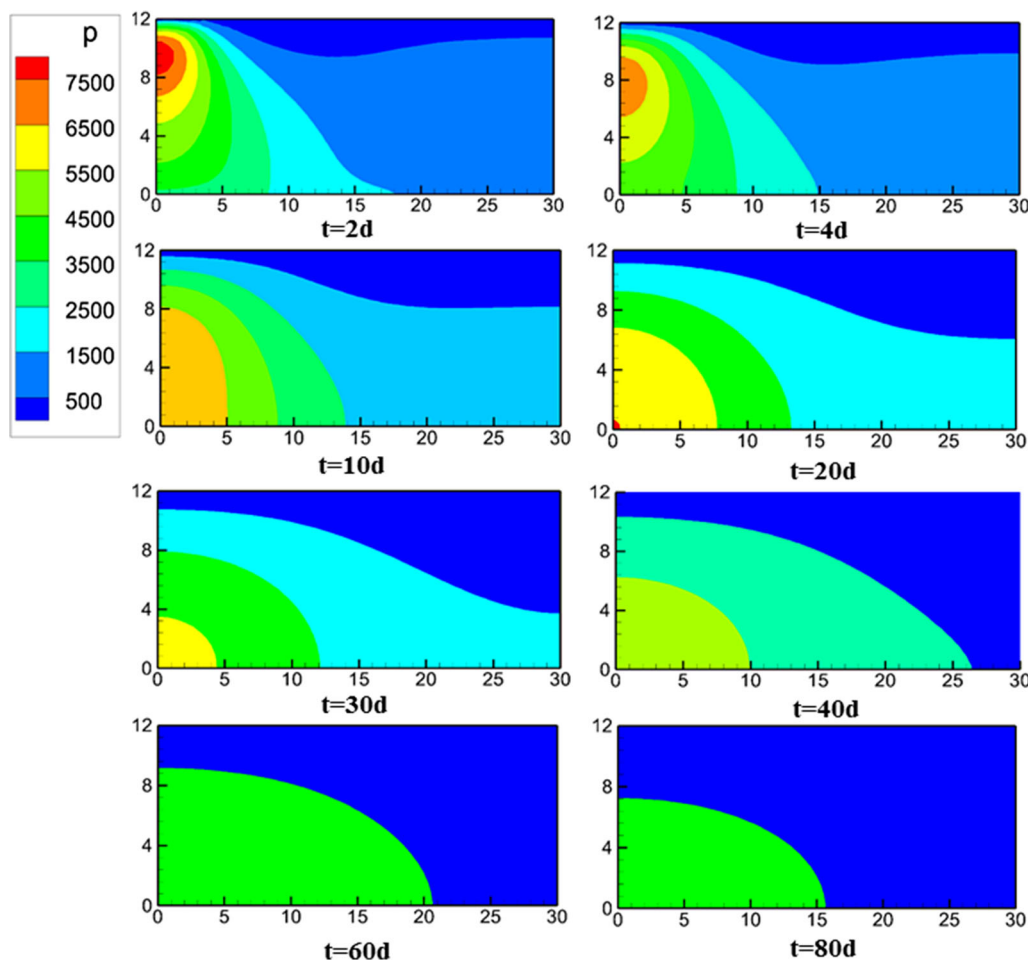
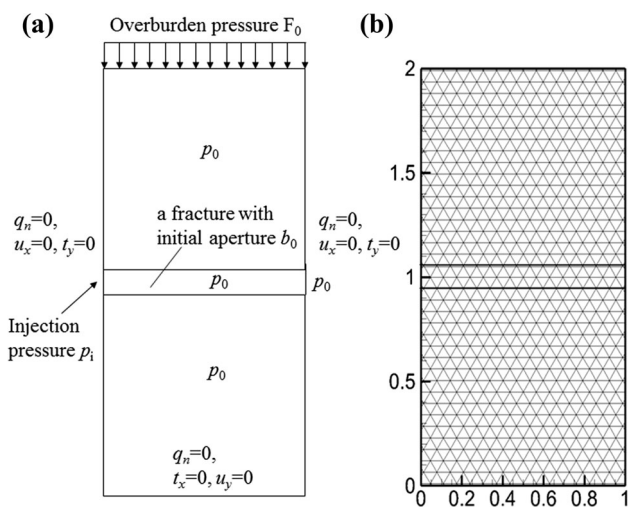Fig. 12 Simulated fluid pressure (Pa) distribution at different times

Fig. 13 Schematic of **a** the numerical model, the boundary conditions and **b** the mesh

nonlinear normal closure behavior with changing normal stiffness. We get the final results with a mechanical fracture aperture of 6×10^{-5} m (60 μm) at the final steady state, which is accurate according to Eq. (8) (because the initial stress is -8 MPa, $\sigma_{n0}' = -5$ MPa, and the initial mechanical aperture is 1×10^{-4} m, while the final stress is -10 MPa. Therefore, according to Eq. (8), the final mechanical aperture should be: $(-8 \times 10^6 + 5 \times 10^6) \times 1 \times 10^{-4}/(-10 \times 10^6 + 5 \times 10^6) = 6 \times 10^{-5}$ m). Then we conducted a simulation considering only indirect coupling, i.e., we deactivate the fluid–solid interaction terms for direct coupling associated with Eqs. (33) and (34). In this case, the coupling occurs only one way, i.e., mechanical deformation affects permeability, but there are no influences of fluid pressure on mechanical field. The mechanical and hydraulic property changes of the fracture under loading and injection with constant pressure of 8 MPa at the left end of the fracture zone and the pressure at the right end of the fracture zone are fixed at zero. Lastly, we run our full package considering both direct and indirect couplings. We output some of the results in Figs. 14 and 15.

We compare the distribution of fluid pressure in cases without considering coupling, only considering indirect

Table 2 Computation parameters for coupled modeling of the constant pressure injection in rock domain with a fracture zone in Fig. 13

Material	Parameter	Value
Fluid	Mass density (ρ_f)	1000 kg/m³
	Dynamic viscosity (μ_f)	1×10^{-3} Ns/m²
Rock matrix	Young's modulus	4 GPa
	Poisson's ratio	0.2
	Permeability coefficient	5×10^{-9} m/s
	Biot–Willis coefficient (α)	1
	Biot's modulus (M)	∞
	Initial vertical effective stress	-8 MPa
Fracture zone	Mass density	2300 kg/m³
	Initial normal effective stress	-8 MPa
	Bandis' parameter (σ_{n0}')	-5 MPa
	Initial thickness of fracture zone	0.1 m
	Initial mechanical aperture of fracture	0.1 mm
	Shear constant (ζ)	10^{-11} Pa^{-1}
	Shear constant (Ψ)	0
	Factor (f)	0.5
	Residual hydraulic aperture (b_{hr})	0
	Biot–Willis coefficient (α)	1
	Biot's modulus (M)	∞
Penalty spring	Stiffness	1.6×10^{11} N/m

coupling and considering both direct and indirect coupling, respectively, as shown in Fig. 14. The difference of fluid pressure distribution between Fig. 14a, b is not obvious, indicating that a steady state is reached for only considering indirect coupling after 30-day injection. However, in Fig. 14c, a steady state has not reached and fluid continues to dissipate from the left to right. This difference could be explained by that in figure b with only indirect coupling, a steady state is reached when mechanical deformation no longer occurs, whereas in case for Fig. 14c, the final steady state will be reached till a balance is reached between the interaction of mechanical and fluid flow fields. Overall, the effects of pressure on solid deformation are not obvious. Further, we compare the aperture change with time at the injection point under these two conditions, shown in Fig. 15. Ignoring the no more than 1.7 % oscillations due to penalty method for material interface conditions in mechanical analysis, we see that the aperture at the final stage reduces to 6×10^{-5} m (60 μm) when only considering indirect coupling. This value is the same as the one in the case of pure mechanical analysis, proving its verification. However, when considering both direct and indirect couplings, the aperture remains steady at 6.5×10^{-5} m (65 μm) under the effect of fluid pressure on the solid skeleton.

5.4 Example 4: NMM analysis of coupled HM processes under constant injection in rock mass with a single dominant fracture

Using the similar material properties as in Example 3 listed in Table 3, we enlarge the model dimension to 10 m × 10 m with the 0.1 m fracture zone in the middle (Fig. 16). The model is initially balanced with 10 MPa initial stress, and we inject fluid at the left end of the fracture zone with a constant pressure of 1 MPa. The right end pressure is set as 0. We conduct this modeling for studying the changing processes of fluid flow pressure and deformation in fracture zone and surrounding rock.

Figure 17 shows the fluid pressure distribution in the whole domain at different times after the start of the injection. We find that the pressure distribution is not symmetric from the left to right during the transient phase just after injection while becomes symmetric after 20 days of injection, indicating that a steady state has been reached. We further choose points A, B, C located within the fracture zone at (1, 5), (2, 5) and (5, 5), respectively, to see the pressure evolution (Fig. 18). We observe an increase of pressure due to injection for each point and then reach steady after 10 days of injection.

In order to study the local hydro-mechanical behavior in the fracture, we extract a profile located at $y = 5.01$ m of the fluid pressure distribution at different times, as shown in Fig. 19. We see that from the beginning till 7 days after injection, the pressure tends to distribute linearly along the fracture, indicating that a steady state is reached.

The vertical displacements relative to the mechanical fixed bottom boundary are shown in Fig. 20. The vertical displacement responds to vertical strain caused by the pressure changes that are first progressing along the fracture from the left to the right and also by fluid pressure diffusion into the surround rock that causes deformations both within the fracture and in the surrounding rock (Fig. 17). Because of that, we see uplift in the entire domain under effects of fluid diffusion and expand the porous system with mechanically fixed bottom and free upper boundaries. The final total uplift at the top boundary is 6 cm, and most of this uplift is caused by the vertical expansion taking place within the rock surrounding the fracture zone. Nevertheless, this example demonstrates the ability of the model to simulate transient HM processes in a fractured rock mass during fluid injection into a dominant flow feature.

Corresponding to Fig. 20, we show the evolution of vertical displacement at profile $x = 1.0$ m in Fig. 21. We obviously see that the vertical displacement increases due to expansion under increasing fluid pressure and reaches steady state after 7 days.
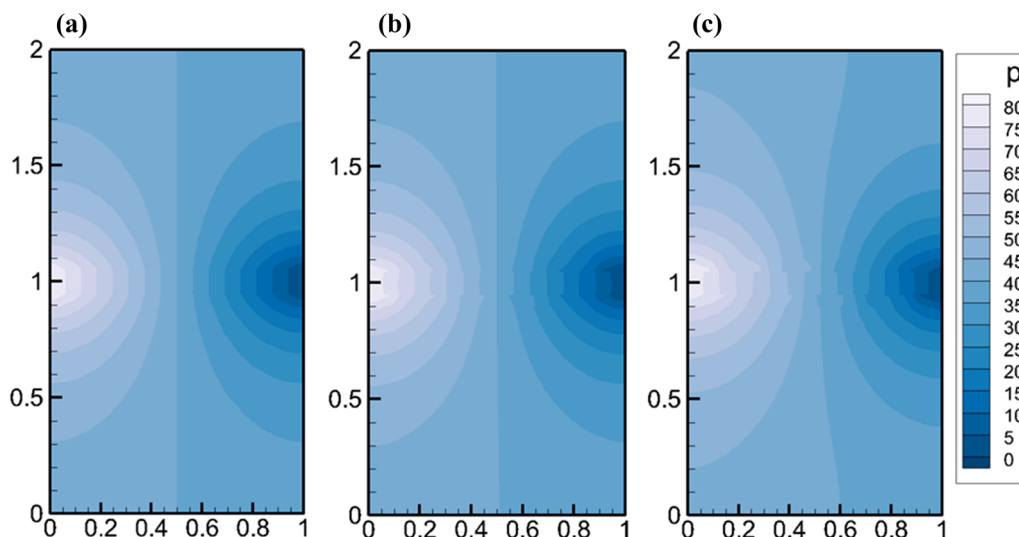
Fig. 14 Distribution of fluid pressure head (m) for **a** flow analysis without considering coupled effects, 30 days after injection, **b** only considering indirection coupling and **c** considering both direct and indirect coupling
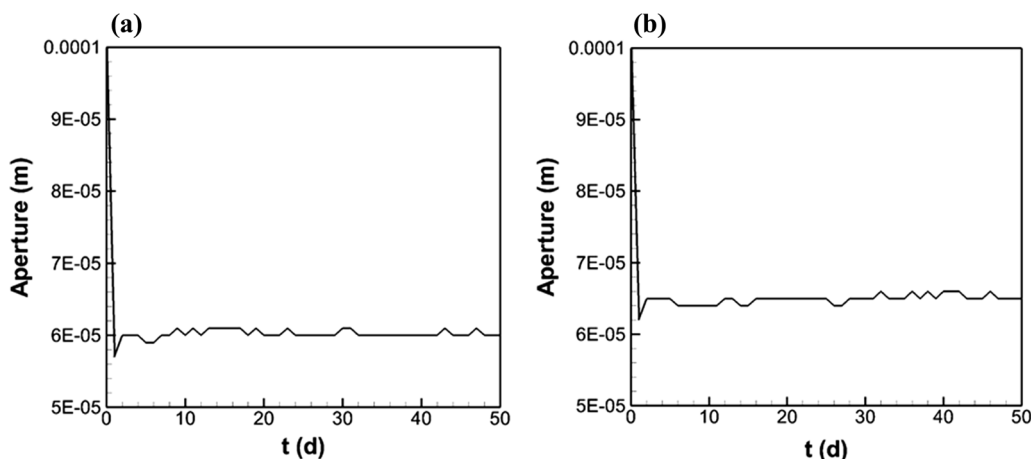

Fig. 15 Aperture change with time at the injection point in simulation **a** only considering indirect coupling and **b** considering both direct and indirect coupling

6 Conclusions and Perspectives

In this study, we developed a new NMM model for coupled hydro-mechanical processes in porous rock containing dominant fractures. We used an approach to model fractures as finite-thickness flow features, or fracture zones, considered as porous media that possesses similar behavior to that of the surrounding rock under direct coupling. However, fracture zones are distinguished from the surrounding rock because of their nonlinear behavior of hydraulic and mechanical properties, as they are very sensitive to deformation. This new model includes:

- A new formulation for analyzing direct HM coupling in porous media. Based on an energy-work model, we stringently established all components of the work

related to fluid flow and mechanical processes in a unified form and their interaction appeared as a direct coupling and these work components are consistent with Biot's equations together with initial and boundary conditions.

- A finite-thickness fracture-zone model with an accurate implicit technique to account for indirect coupling associated with changes in the nonlinear hydraulic and mechanical properties of the fractures. We proposed a new model denoted finite-thickness fracture zone representing the composite effect of a dominant fracture, mineral fillings and part of adjacent rock matrix, with both linear and nonlinear constitutive features. We derived an implicit formulation by directly assembling the corresponding strain energy to consider the

Table 3 Computation parameters for coupled modeling of the constant pressure injection in rock domain with a fracture zone in Fig. 16

Material	Parameter	Value
Fluid	Mass density (ρ_f)	1000 kg/m³
	Dynamic viscosity (μ_f)	1×10^{-3} Ns/m²
Rock matrix	Young's modulus	100 MPa
	Poisson's ratio	0.2
	Permeability coefficient	5×10^{-9} m/s
	Biot–Willis coefficient (α)	1
	Biot's modulus (M)	∞
	Initial vertical effective stress	-10 MPa
Fracture zone	Mass density	2300 kg/m³
	Initial normal effective stress	-10 MPa
	Bandis' parameter (σ_{n0}')	-2 MPa
	Initial thickness of fracture zone	0.1 m
	Initial mechanical aperture of fracture	0.1 mm
	Shear constant (ζ)	10^{-8} Pa^{-1}
	Shear constant (Ψ)	0
	Factor (f)	0.5
	Residual hydraulic aperture (b_{hr})	0
	Biot–Willis coefficient (α)	1
	Biot's modulus (M)	∞
Penalty spring	Stiffness	4.0×10^{10} N/m

nonlinear properties of the fracture zones. Compared with traditional approximations of the nonlinear constitutive equations, this new formulation achieves more accurate representation of the nonlinear behavior.

- Implementation in NMM with unconstructed mathematical mesh, cover-based approximation and simplex integration. We implemented this new formulation in NMM. With unconstructed mathematical mesh in NMM, meshing efficiency could be dramatically reduced. With the cover-based approximation, instead of nodal-based approximation, the approximation order could be flexibly increased for intense changes around fractures. With simplex integration, high accuracy could be achieved on arbitrarily shaped polygons.

- An implicit time-marching algorithm and an incremental formulation to solve the displacements and initial stress for this strongly nonlinear problem. We used the incremental formulation for solving the displacements and initial stress in different time steps and implicit time-marching algorithm for better accuracy of this nonlinear problem. With the new model, we developed a new computer code in our NMM package.

We first simulated a classical poroelastic problem of a column under loading and compared the results with the analytical solution derived by Biot. We found excellent agreement of our NMM solution with very coarse mesh with Biot's analytical solution, showing the accuracy and efficiency of our formulation for direct coupling. Then we modeled a poroelastic problem of an infinite layer under loading and showed the processes of displacement changes and fluid pressure dissipation with exact agreement to an analytical solution. We tested the new model on a model with a single dominant fracture. As the direct coupling was verified in the two first examples, we compared the results of a case considering the fracture with only indirect coupling and the results of a case considering the fracture as nonlinear porous media with both direct and indirect couplings. We found reasonable results from these comparisons and showed the importance of full consideration of both direct and indirect couplings in coupled HM analysis involving dominant flow features.

The approach established in this analysis for the modeling of finite-thickness dominant flow features is a continuous equivalent porous media with strongly nonlinear properties. The flow features can be conveniently discretized explicitly within the fixed mathematical mesh, and the boundary
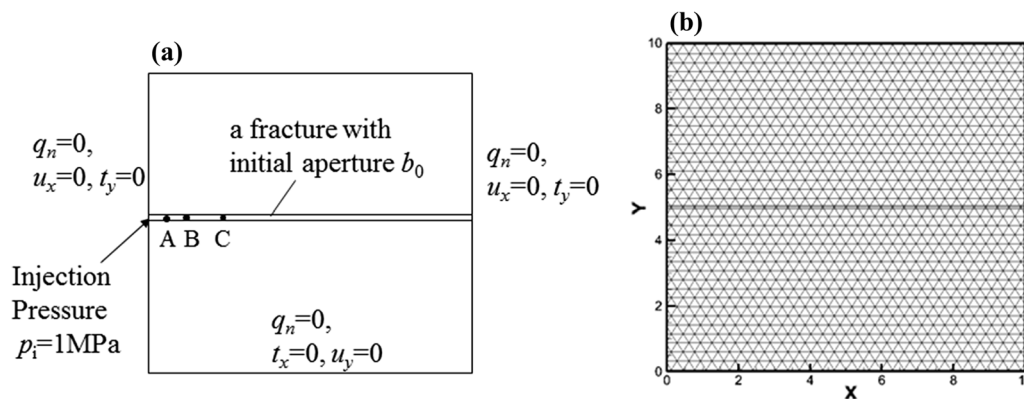

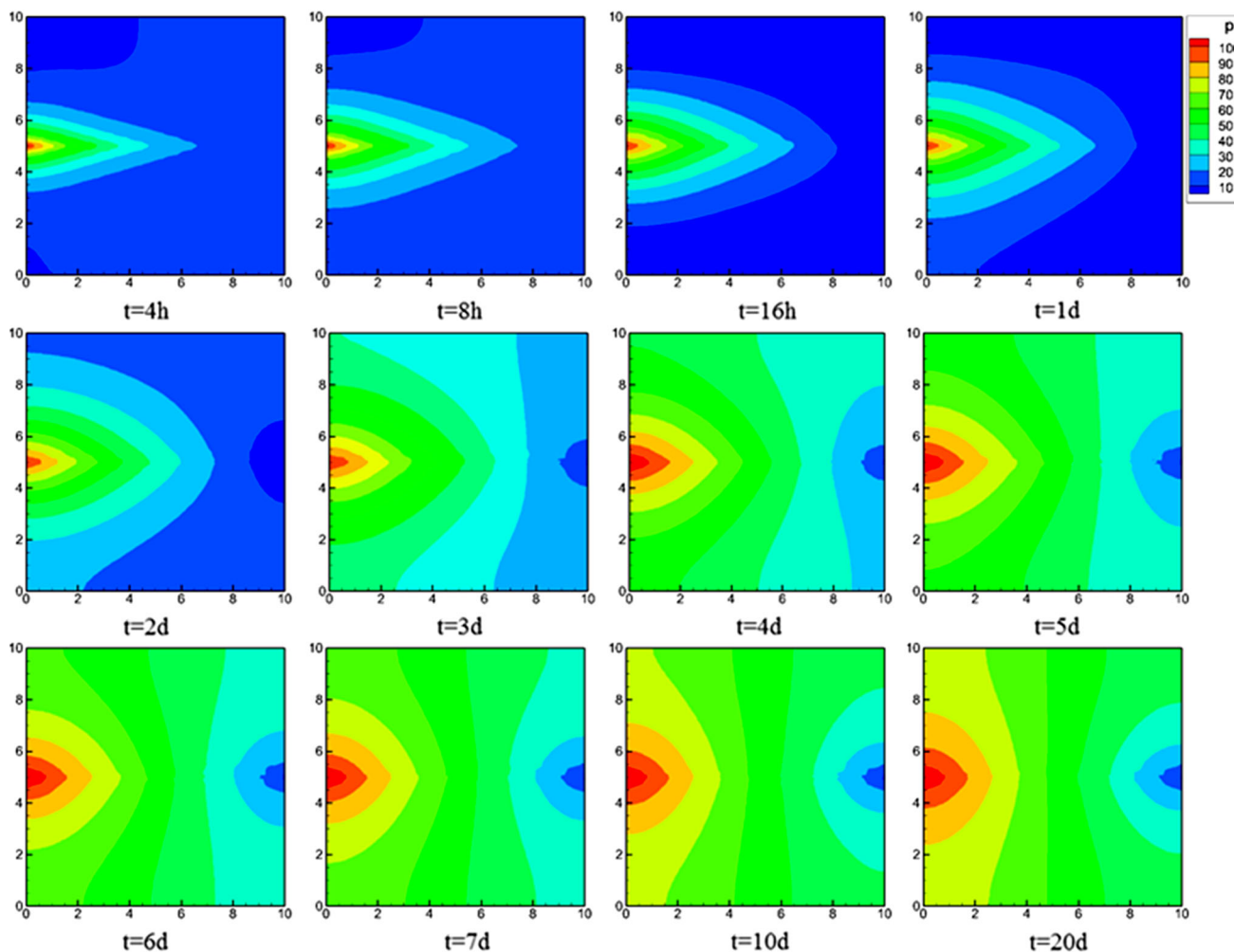**Fig. 16** Schematic of **a** the numerical model, the boundary conditions and **b** the mesh

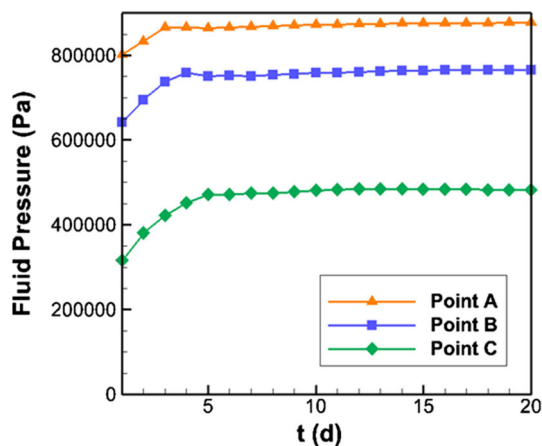**Fig. 17** Simulated fluid pressure head (m) distribution at different times

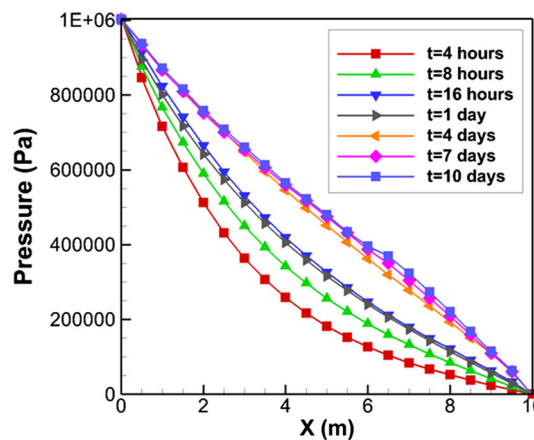**Fig. 18** Evolution of fluid pressure at points A, B and C

Fig. 19 Evolution of fluid pressure distribution of profile $y = 5.01$ m

conditions are realized by penalty method and Lagrange multiplier method for mechanical and fluid flow analysis, respectively. This method is suitable for modeling dominant flow features in a fracture rock mass, including major fractures, and minor faults as well as major faults. In the case of faults, the cross-fault permeability can be
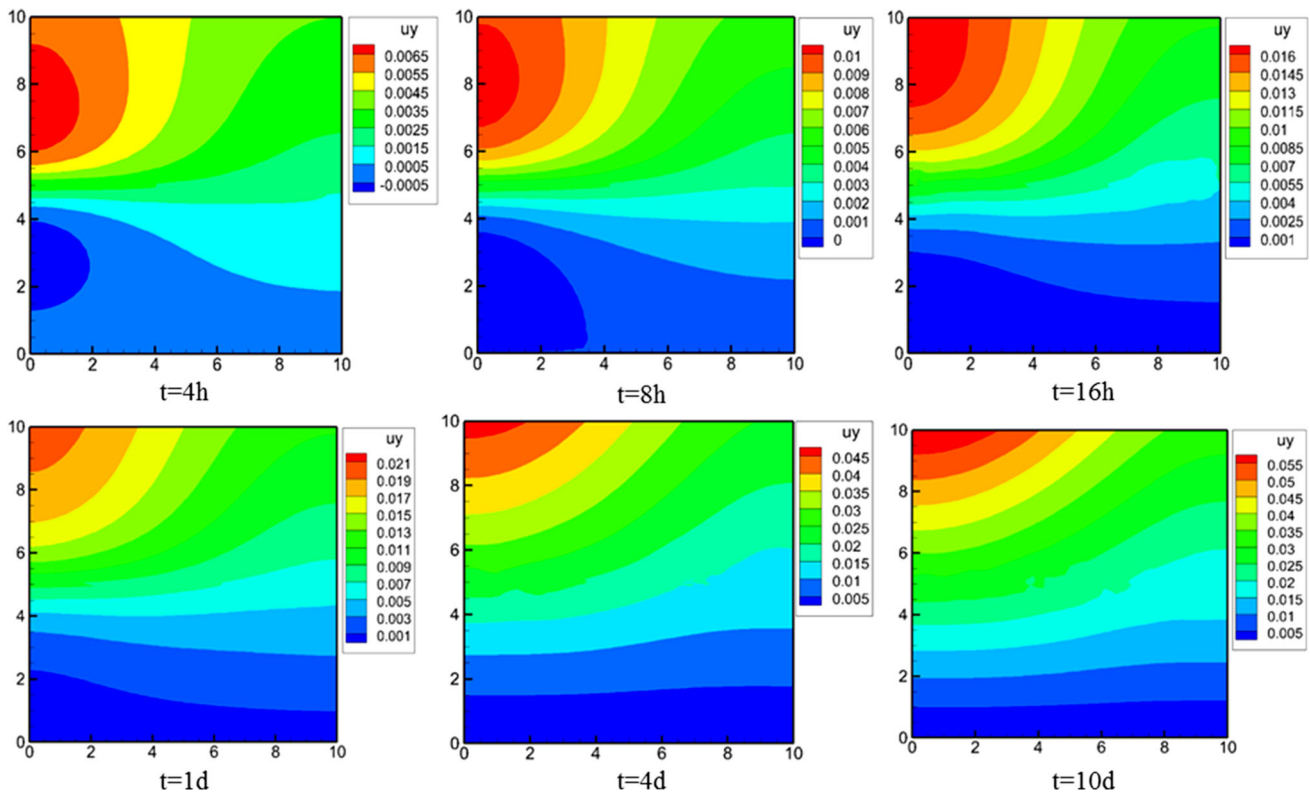
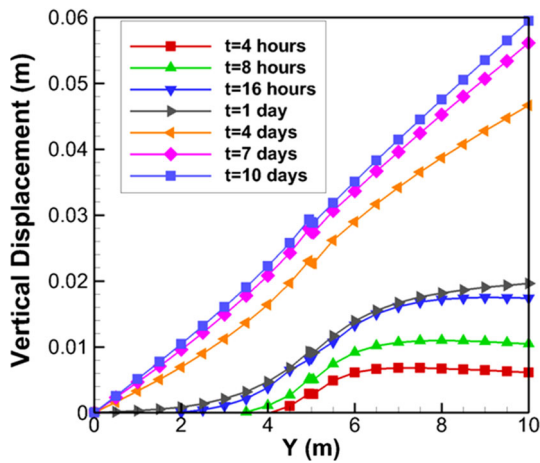**Fig. 20** Contour of vertical displacement at different times

Fig. 21 Evolution of vertical displacement at profile $x = 1.0$ m

substantially different from the along-fault permeability, including the effects of a permeable damage zone and an impermeable fault core. Such difference in cross-fault versus along-fault mechanical and hydraulic properties could be readily modeled using the finite-thickness continuous modeling approach. However, for modeling small-scale, thin unfilled fractures, an alternative discontinuous approach may be preferable. In that case, the fluid flow will be conducted mainly in the direction along the fractures and interaction between fractures and surrounding rock is by fluid pressure and continuity of displacements on the surfaces of fractures. Together with further development for thin fractures, the new model presented in this study can provide a comprehensive model applicable for coupled HM analysis fractured rock masses, including a wide range of flow features.

7 Appendix: Derivation of the effective normal stress in the nonlinear finite-thickness fracture zone

The finite-thickness fracture zone contains the linear and nonlinear part, and the strain in normal direction can be expressed as:

$$\varepsilon_n^{(ii)} = \eta\delta\sigma_n^{\prime(ii)} + \frac{b_m^{(ii)} - b_m^{(ii-1)}}{I_d^{(ii-1)}} \tag{87}$$

Combining Eqs. (8), (87) becomes

$$\varepsilon_n^{(ii)} = \eta\delta\sigma_n^{\prime(ii)} + \frac{\frac{\xi}{\sigma_n^{\prime(ii)} - \sigma_{n0}'} - \frac{\xi}{\sigma_n^{\prime(ii-1)} - \sigma_{n0}'}}{I_d^{(ii-1)}} \tag{88}$$

Denoting $x = \varepsilon_n^{(ii)} + \frac{\xi}{\left[\sigma_n^{\prime(ii-1)} - \sigma_{n0}'\right] I_d^{(ii-1)}}$, Eq. (88) becomes

$$x = \eta\left[\sigma_n^{\prime(ii)} - \sigma_n^{\prime(ii)-1}\right] + \frac{\xi}{\left[\sigma_n^{\prime(ii)} - \sigma_{n0}'\right] I_d^{(ii-1)}} \tag{89}$$

Equation (89) further becomes a quadratic equation:

$$\eta\left[\sigma_n^{\prime(ii)}\right]^2 - \left[\eta\sigma_n^{\prime(ii-1)} + \eta\sigma_{n0}' + x\right]\sigma_n^{\prime(ii)}$$
$$+ \left[\eta\sigma_n^{\prime(ii-1)}\sigma_{n0}' + x\sigma_{n0}' + \frac{\xi}{I_d^{(ii-1)}}\right] = 0 \tag{90}$$

The solution of Eq. (90) is

$$\sigma_n^{\prime(ii)} = \frac{\left[\eta(\sigma_n^{\prime(ii-1)} + \sigma_{n0}') + x\right]}{2\eta}$$
$$\pm \frac{1}{2\eta}\sqrt{\begin{array}{l} \left[\eta(\sigma_n^{\prime(ii-1)} + \sigma_{n0}') + x\right]^2 \\ -4\eta\left[\eta\sigma_n^{\prime(ii-1)}\sigma_{n0}' + x\sigma_{n0}'\right] \\ -4\eta\frac{\xi}{I_d^{(ii-1)}}\end{array}} \tag{91}$$

And it is further expressed as:

$$\sigma_n^{\prime(ii)} = \frac{\left[\eta\left(\sigma_n^{\prime(ii-1)} + \sigma_{n0}'\right) + x\right]}{2\eta}$$
$$\pm \frac{\sqrt{\left[\eta\left(\sigma_n^{\prime(ii-1)} - \sigma_{n0}'\right) + x\right]^2 - 4\frac{\xi}{I_d^{(ii-1)}}\eta}}{2\eta} \tag{92}$$

When $\eta = 0$, only nonlinear feature of the fractures is considered. When $\xi = 0$, only linear feature of the fractures is considered. Therefore, we have:

$$\sigma_n^{\prime(ii)} = \frac{\left[\eta\left(\sigma_n^{\prime(ii-1)} + \sigma_{n0}'\right) + x\right]}{2\eta}$$
$$- \frac{\sqrt{\left[\eta\left(\sigma_n^{\prime(ii-1)} - \sigma_{n0}'\right) + x\right]^2 - 4\frac{\xi}{I_d^{(ii-1)}}\eta}}{2\eta} \tag{93}$$

References

1. An XM, Li LX, Ma GW, Zhang HH (2011) Prediction of rank deficiency in partition of unity-based methods with plane triangular or quadrilateral meshes. Comput Methods Appl Mech Eng 200:665–674
2. Bandis S, Lunsden AC, Barton NR (1983) Fundamentals of rock joint deformation. Int J Rock Mech Min Sci Geomech Abstr 29:249–268
3. Biot MA (1941) General theory of three dimensional consolidation. J Appl Phys 12:155–164
4. Bower KM, Zyvoloski G (1997) A numerical model for thermo-hydro-mechanical coupling in fractured rock. Int J Rock Mech Min Sci Geomech Abstr 34:1201–1211
5. Chen GQ, Ohnishi Y, Ito T (1998) Development of high-order manifold method. Int J Numer Methods Eng 43:685–712
6. Duncan JM, Chang CY (1970) Nonlinear analysis of stress–strain in soils. J Soil Mech Found Div ASCE 96(SM5):1629–1653
7. Goodman RE (1974) The mechanical properties of joints. In: Advances in rock mechanics: proceedings of the third congress of the international society for rock mechanics, pp. 127–140
8. Goodman RE (1976) Methods of geological engineering in discontinuous rocks. West Publishing, New York
9. Guvanasen V, Chan T (1995) A new three-dimensional finite-element analysis of hysteresis thermohydromechanical deformation of fractured rock mass with dilatance in fractures. In: Proceedings of the second conference on mechanics of jointed and faulted rocks. Vienna April 10–14, pp. 347–442
10. Hu M, Wang Y, Rutqvist J (2015) On continuous and discontinuous approaches for modeling groundwater flow in heterogeneous media using the numerical manifold method: model development and comparison. Adv Water Resour 80:17–29
11. Itasca Consulting Group (2011) UDEC Manual: Universal Distinct Element Code version 5.0 Minneapolis, MN, USA
12. Itasca Consulting Group (2013) 3DEC (Advanced, Three Dimensional Distinct Element Code), Version 5.0, Minneapolis, MN, USA
13. Jing LR, Ma Y, Fang ZL (2001) Modeling of fluid flow and solid deformation for fractured rocks with discontinuous deformation analysis (DDA) method. Int J Rock Mech Min Sci 38(3):343–355
14. Kim Y, Amadei B, Pan E (1999) Modeling the effect of water, excavation sequence and rock reinforcement with discontinuous deformation analysis. Int J Rock Mech Min Sci 36(7):949–970

15. Kohl T, Hopkirk RJ (1995) The finite element program "FRACTure" for the simulation of hot dry rock reservoir behavior. Geothermics 24:345–359

16. Ling SD, Ye M (2005) Manifold element method for Biot's plane consolidation analysis. Chin J Comput Mech 22(3):274–280

17. Ma GW, An XM, He L (2010) The numerical manifold method: a review. Int J Comput Methods 7(1):1–32

18. McNamee J, Gibson RE (1960) Plane strain and axially symmetric problems of the consolidation of a semi-infinite clay stratum. Q J Mech Appl Math 13:210–227

19. Nguyen TS (1996) Description of the computer code FRACON. In: Stephansson O, Jing L, Tsang C-F (eds) Coupled thermo-hydro-mechanical processes of fractured media, vol 79. Elsevier, Amsterdam, pp 539–544 (**Developments in Geotechnical Engineering**)

20. Nguyen TS, Selvadurai APS (1995) Coupled thermal-hydrological- mechanical processes in sparsely fractured rock. Int J Rock Mech Min Sci Geomech Abstr 32:465–480

21. Noorishad J, Ayatollahi MS, Witherspoon PA (1982) Coupled stress and fluid flow analysis of fractured rock. Int J Rock Mech Min Sci 19:185–193

22. Noorishad J, Tsang CF, Witherspoon PA (1992) Theoretical and field studies of coupled hydromechanical behavior of fractured rock–1. Development and verification of a numerical simulator. Int J Rock Mech Min Sci 29(4):401–409

23. Ohnishi Y, Kobayashi A (1996) THAMES. In: Stephansson O, Jing L, Tsang C-F (eds) Coupled thermo-hydro-mechanical processes of fractured media, vol 79. Elsevier, Amsterdam, pp 545–549 (**Developments in Geotechnical Engineering**)

24. Ohnishi Y, Shibata H, Kobayashi A (1987) Development of finite element code for the analysis of coupled thermo-hydro-mechanical behavior of a saturated-unsaturated medium. In: Tsang C-F (ed) Coupled processes associated with nuclear waste repositories. Academic Press, Orlando, pp 679–696

25. Pine RJ, Cundall PA (1985) Application of the fluid rock interaction program (FRIP) to the modeling of hot dry rock geothermal energy systems. In: Stephansson O (ed) Proceedings of the international symposium on fundamentals of rock joints. Centek Publishers, Lulea, pp 293–302

26. Rutqvist J, Stephansson O (2003) The role of hydromechanical coupling in fractured rock engineering. Hydrogeol J 11(1):7–40

27. Rutqvist J, Noorishad J, Tsang CF (1998) Determination of fracture storativity in hard rocks using high-pressure injection testing. Water Resour Res 34(10):2551–2560

28. Rutqvist J, Tsang CF, Stephansson O (2000) Uncertainty in the maximum principal stress estimated from hydraulic fracturing measurements due to the presence of the induced fracture. Int J Rock Mech Min Sci 37:107–120

29. Rutqvist J, Borgesson L, Chijimatsu M, Jing L, Nguyen ST, Noorishad J, Tsang C-F (2001) Thermohydromechanics of partially saturated geological media: governing equations and formulation of four finite element models. Int J Rock Mech Min Sci 38(1):105–127

30. Shi GH (1992) Manifold method of material analysis. In: Transaction of the 9th army conference on applied mathematics and computing, U.S. Army Research Office

31. Shi GH (1996) Simplex integration for manifold method, FEM, DDA and analytical analysis. In: Salami MR, Bank D (eds) Discontinuous deformation analysis (DDA) and simulations of discontinuous media. TSI press, Albuquerque, pp 205–262

32. Silvestre JR, Vargas EA, Vaz LE, Soares AC (2015) Modelling of coupled fluid-mechanical problems in fractured geological media using enriched finite elements. Int J Numer Anal Methods Geomech 39:1104–1140

33. Swenson DV, DuTeau R, Sprecker T (1997) A coupled model of fluid flow in jointed rock applied to simulation of a hot dry rock reservoir. Int J Rock Mech Min Sci Geomech Abstr 34:308

34. Wang Y (1995) Seepage flow analysis and seepage-stress coupled analysis of fissured rock masses. Ph.D. Dissertation, Hohai University

35. Wang HF (2000) Theory of linear poroelasticity. Princeton University Press, Princeton

36. Wang Y, Su BY, Xu ZY (1998) Coupling analysis of seepage and stress in multi-fractured rock masses. J Hohai Univ 26(2):26–30

37. Wang Y, Xu ZY, Su BY (1998) Four- freedom complete method for the seepage-stress coupled analysis in fissured rock masses. Hydraul J 7:55–59

38. Wang Y, Hu M, Zhou Q, Rutqvist J (2014) Energy-work-based numerical manifold seepage analysis with an efficient scheme to locate the phreatic surface. Int J Numer Anal Methods Geomech 38:1633–1650

39. Witherspoon PA, Wang JSY, Iwai K, Gale JE (1980) Validity of the cubic law for fluid flow in a deformable fracture. Water Resour Res 16:1016–1024

40. Zhang HW, Zhou L (2006) Numerical manifold method for dynamic nonlinear analysis of saturated porous media. Int J Numer Anal Methods Geomech 30:927–951

41. Zienkiewicz OC, Qu S, Taylor RL, Nakazawa S (1986) The patch test for mixed formulation. Int J Numer Methods Eng 23:1873–1883

42. Zienkiewicz OC, Huang MS, Wu SM (1993) A new algorithm for the coupled soil-pore fluid problem. Shock Vib 1(1):3–14